



Compact 3D Microscopy for Planetary Exploration

GUSTAV PETTERSSON

Master of Science Thesis

KTH Royal Institute of Technology
School of Engineering Sciences
100 44 Stockholm, Sweden

Conducted at:

NASA Ames Research Center
Moffett Field, CA 94035, USA

Presented: 23 May 2018

KTH Examiner and Supervisor: Gunnar Tibert
NASA Mentors: Michael Dille and Uland Wong

Abstract

We propose using grain-of-sand-scale microscopy (1-micrometre resolution) to study the microstructure and composition of planetary material in a fast, in-situ, solid-state device. We have constructed a small and light prototype instrument (100 grams, 0.3 litres) from commercial-off-the-shelf components, targeted for applications in miniaturised robotic exploration, mounted to a robotic arm, or used as a hand-held tool. This microscope employs a programmable LCD aperture to virtually record multiple perspectives, and a dome studded with LEDs surrounding the sample to control illumination. With this prototype microscope we have captured rich and intuitive raw images for a human observer, and reconstructed 3D surfaces and photometric properties of the samples. The broad applicability of this method is demonstrated by integration into a novel exploration concept in which sensor projectiles are launched from a rover into inaccessible environments. Our microscope can there deliver 3D-maps of the surfaces they encounter and extract relevant morphological properties. Our prototype device is evaluated using a range of lunar and planetary simulants. We argue that this microscope delivers large scientific value on its own, and context for other instruments, with small resource requirements similar to those of a camera alone.

Sammanfattning

Vi presenterar en metod där mikroskopi med mikrometerupplösning används för att studera mikrostruktur och sammansättning på ytan av planeter. En liten och lätt prototyp (ca. 100 gram, 0.3 liter) av detta mikroskop konstrueras av kommersiellt tillgängliga komponenter och utan rörliga delar. Det är speciellt anpassat för applikationer inom robotik eller som ett handhållet instrument. Mikroskopet använder en programmerbar LCD-apertur för att virtuellt fånga bilder från flera perspektiv samt en kupol med lysdioder för att styra belysningen av provet. Med denna prototyp har vi genererat detaljrika och intuitiva rådata för människor samt implementerat metoder för att rekonstruera 3D-formen och de fotometriska egenskaperna hos provet. Vi understryker användbarheten genom att integrera prototypen i ett nytt koncept för utforskning av planeter, där instrumentet monteras i projektiler som avfyras från en strövsare till annars oåtkomliga platser. Därifrån levererar vårt mikroskop 3D-formen samt relevanta morfologiska data om den ytan som påträffas. Vi utvärderar metoden vidare med en uppsättning material som liknar regolit från Månen respektive Mars. Vi anser att denna metod levererar stort vetenskapligt värde samtidigt som den har små resursbehov liknande en enkel kameran.

Acknowledgements

I am grateful for the support of the Swedish National Space Board which enabled my visit to the NASA Ames Research Center. The work on the SPEARS project was funded by the NASA Ames Center Innovation Fund (CIF) 2017 and Internal Research & Development Program (IRAD) 2018.

I deeply appreciate the trust, support, and mentoring of Michael Dille and Uland Wong at NASA during this work, and my advisor Gunnar Tibert at KTH. I also want to thank Babak Hassibi at Caltech, Hjalmar Brismar and Sven Grahn at KTH, and Sara Abrahamsson at UC Santa Cruz for supporting and encouraging my spurious research interests over the years. You have each played a vital part in my past and helped me find my path for the future. It has been an honour and a privilege to find myself in your company; I would be nowhere without you and I wish each of you success in all of your endeavours.

Sist men inte minst, till min familj: Vi ses för sällan.

Contents

1	Introduction	1
1.1	Background	1
1.2	The SPEARS project	2
1.3	Thesis purpose and contribution	2
2	3D Microscopy	4
2.1	Microscopy basics	4
2.2	Light field microscopy	6
2.3	Controlled illumination microscopy	9
2.3.1	Contrast and specularity enhancement	9
3	Demonstrator microscope	11
3.1	Optical table setup	11
3.2	Light field microscopy in practice	13
4	Shape reconstruction	17
4.1	Light field to surface height	17
4.1.1	Disparity correlation	17
4.1.2	Pyramid filtering of disparity	20
4.1.3	Disparity to physical height	22
4.2	Controlled illumination to surface normal	23
4.3	Combining disparity and normals	25
4.3.1	Correcting normals	26
4.3.2	Correcting disparity	26
5	Data analysis	29
5.1	Visually apparent data	29
5.2	Particle size in z-direction	29
5.3	Void fraction	30
5.4	Specularity	30
6	Miniaturised microscope	32
6.1	Future development	34
7	Conclusions and future work	35
A	Regolith measurement data	37
A.1	JSC MARS-1 (small particles)	38
A.2	JSC MARS-1 (medium particles)	39

A.3 JSC MARS-1 (large particles)	40
A.4 JSC-1A (small particles)	41
A.5 JSC-1A (medium particles)	42
A.6 JSC-1A (large particles)	43
A.7 NU-LHT-2M (finely milled)	44
A.8 RPBL (finely milled)	45
B Schematics and PCBs	46
B.1 LCD holder	46
B.2 Control electronics	47
Bibliography	51

1 Introduction

1.1 Background

Exploration of bodies in our solar system has taken a giant leap from the first successful lunar lander, the Soviet Union *Luna 9* in 1966. (Incredibly, the first manned landing on the Moon occurred only three years later when the NASA¹ *Apollo 11* touched down in the Sea of Tranquillity.) In the following years, soft landings have been carried out on Venus (Soviet Union *Venera 7*, 1970), Mars (Soviet Union *Mars 3*, 1971), Titan (ESA² *Huygens*, 2005), and Comet 67P/C-G (ESA *Philae*, 2015) [Williams, 2018].

Since the NASA *Sojourner* landed on Mars in 1997 [Williams, 2018] the state-of-the-art in planetary exploration has remained the car-like multi-purpose rovers. With these, the plains of Mars have been explored and studied in detail with precise instruments carried onboard and auxiliary help from e.g. drills, scoops, and lasers. With current rover design, possible places to explore are limited to smooth and packed nearby terrain where the risk of damage or embedding is low. In the near future, we expect the paradigm of exploration to shift focus towards extreme environments which current technology cannot reach. This is clear from recently proposed concepts to roll [Bruce, 2016], hop [Howe et al., 2011], scatter [Harri et al., 2017], or fly [Datta et al., 2003] instruments on small and versatile robotic platforms. The limited area coverage of a single rover is a further impediment, emphasised by the small Mars Helicopter Scout (MHS) which will be flown on the upcoming *Mars 2020* mission to help plan the route of the main rover [NASA, 2018]. As exploration is shifting to new environments and methods the instruments must follow suit. In general, the available resources and size of future platforms are limited, making non-mechanical and in-situ instruments which allow mechanically simple robots desirable.

Microscopy for planetary exploration is not a new concept. The *Spirit*, *Opportunity* and *Curiosity* rovers all carried microscopes (Athena Microscopic Imager [Herkenhoff et al., 2003] or Mars Hand Lens Imager [Edgett et al., 2012]) to study structures and provide context for other instruments. The premise of this thesis, however, is for an order of magnitude higher resolution, combined with 3D capture and photometric study. The proposed system is, unlike many other instruments, general in nature. The grain-of-sand-scale

¹National Aeronautics and Space Administration

²European Space Agency

imaging provides intuitive images of an object's microstructure and macro-composition, which gives clues to properties and formation of all materials. Combined with this, quantitative data can be recovered with analysis methods such as photometry and shape reconstruction. This breadth in use is especially important for exploration of unknown territories where specialised instruments may not be as valuable.

1.2 The SPEARS project

SPEARS (Smart Projectiles for Environmental Assessment, Reconnaissance, and Sensing) bridges the gap between classical rovers and extreme environmental exploration. The rover is fitted with a cold-gas launcher and a collection of instruments built into small projectiles are carried on the rover, see Figure 1.1. Different types of projectiles with specific sensing capabilities are designed to provide data tuned for each exploration task. Variants of current instrumentation may be adapted to this enhanced-reach concept but primarily the payloads are envisaged to be uniquely designed to take advantage of the concept. A previously demonstrated example is a local area mapping projectile. It is fitted with a high frame rate camera which records images from the projectile in flight. The images in the sequence which show the ground are then assembled into a high-quality mosaic of the local area.

1.3 Thesis purpose and contribution

This thesis details the development of a 3D microscopy payload for planetary exploration. It is designed to be a small, light, and durable payload suitable to enhance the capabilities of several proposed exploration concepts. As far as we are aware, the general concept of 3D microscopy for planetary exploration is unique. Furthermore, we believe to have demonstrated the smallest ever light field microscope, as well as the first combined light field and controlled illumination microscope.

This thesis is organised as follows: Chapter 2 provides the basics of 3D microscopy. Chapter 3 presents our benchtop demonstrator microscope and Chapter 4 develops methods for object shape reconstruction. Chapter 5 shows some data analysis methods. Chapter 6 presents a miniature version developed for SPEARS with a mass and volume of approximately 100 grams and 0.3 litres. Chapter 7 discusses the impact of the technology, its applicability to exploration, and several avenues of future enhancements.

The technologies developed in this thesis are entered as case number ARC-18239-1 in the NASA Technology Transfer Program with the title: *Miniature 3D Microscope for Field Inspection and Planetary Exploration*.

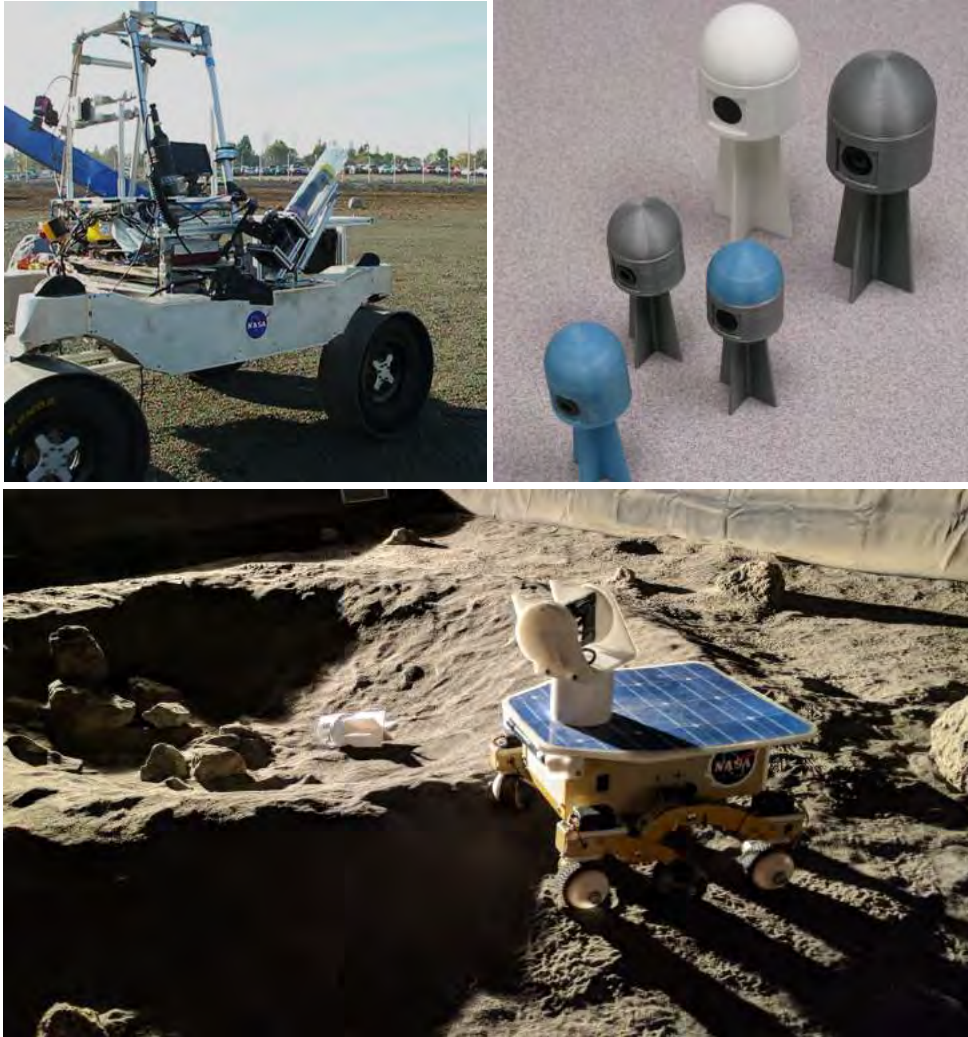


Figure 1.1: Left: Picture of our KREX-2 rover with the SPEARS launcher mounted on the front. Right: A family of SPEARS projectiles. Bottom: Mock-up of a rover parked at the edge of a crater with the projectile sensor from Chapter 6 deployed to the centre.

2 3D Microscopy

Using microscopy as a scientific instrument began long before the space age. Recent developments, such as super-resolution, see [Birk, 2017], atomic force, see [Eaton and West, 2010], and scanning electron, see [Wells, 1974], microscopy have pushed the boundaries for resolution down to the atom-size. Capturing three-dimensional data is also possible. The most common technique is to capture several 2D images separated axially (called slices) and then recovering the 3D volume [Buetow, 1994]. Techniques to capture several slices simultaneously by multifocus microscopes have been demonstrated [Abrahamsson et al., 2012] to improve speed. Capturing 2D slices inside a volume requires the sample to be transparent. When imaging opaque objects the lower layers will be obstructed and full 3D volume reconstruction is limited. Slicing techniques degrade from 3D volume reconstruction to height-map reconstruction (e.g. depth-from-focus [Favaro, 2007]), where only the contour of the top surface is recovered.

In this work we will focus on light field microscopy (LFM) [Levoy et al., 2006] where the angles of the incoming light rays are recorded together with the usual images. This additional information can be used to e.g. shift the focus after the fact [Ng et al., 2005], or recover the height map as we discuss thoroughly in Chapter 4. Additionally, we will consider controlled illumination microscopy (CIM) where images are captured with different light sources and the shadows and highlights are used to recover height information. The combination of these methods provide improved 3D data and also form a gainreflectometer which enables capture of the photometric properties of the sample.

2.1 Microscopy basics

In this Chapter, the fundamental concepts of microscopy which are important to this thesis are presented. We will only consider the thin lens approximation and assume that all lenses are ideal. In reality, every lens considered here is created by several carefully tuned lenses combined to approximate the ideal thin lens. Each lens has two fundamental properties measured in millimetres: a focal length f , and an aperture (or diameter) a . For a detailed discussion of image formation and optical corrections used in microscopy see e.g. [Davidson and Abramowitz, 2002].

The discussion is further limited to infinity-corrected microscopy. This term denotes that the rays exiting the objective are parallel (i.e. focused at infinity).

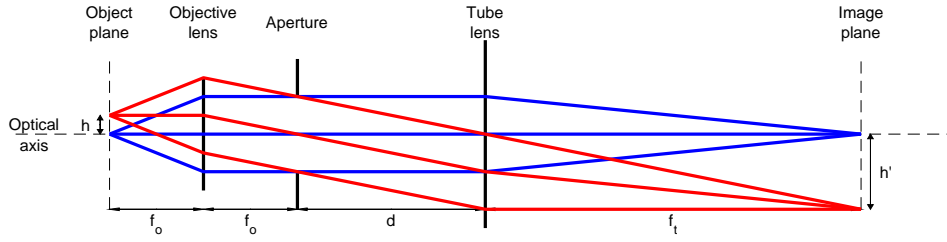


Figure 2.1: Optical train of infinity-corrected microscope.

Figure 2.1 show the optical train, with objective lens, aperture, and tube lens. A third lens (the eyepiece) is often placed to the right of the image plane to relay the image into a human eye. When using digital imaging, the camera sensor is placed in the image plane, and the eyepiece is omitted. To achieve infinity focus the objective lens is placed one focal length f_o away from the sample. The aperture diameter a limits the rays which may pass through the system. It is placed one focal length f_o behind the objective lens to make the system object-space telecentric. The effect is that every part of the sample appears to be imaged from straight above and that moving the sample closer or farther away from the objective does not change its magnification [Levoy et al., 2006]. Next is the tube lens with focal length f_t and the camera sensor placed f_t behind the tube lens. The space between the aperture and the tube lens is called infinity space and the distance d of this space may be varied without changing the properties of the system.¹

There are two important factors determining the performance of the microscope. The magnification M :

$$M = \frac{h'}{h} = \frac{f_t}{f_o} \quad (2.1)$$

And the numerical aperture NA , defined by the maximum angle of light which can be captured: (see Figure 2.2)

$$NA = \sin(\theta) \quad \text{where} \quad \tan(\theta) = \frac{a}{2f_o} \quad (2.2)$$

A microscope with a large NA will gather more light. It will also produce a shallower depth-of-focus (DOF), Δz . The DOF of an ideal microscope is given by [Spring and Davidson]:

$$\Delta z = \frac{\lambda}{NA^2} + \frac{\Delta xy}{M \cdot NA} \quad (2.3)$$

¹This is the reason all modern microscopes are infinity-corrected.

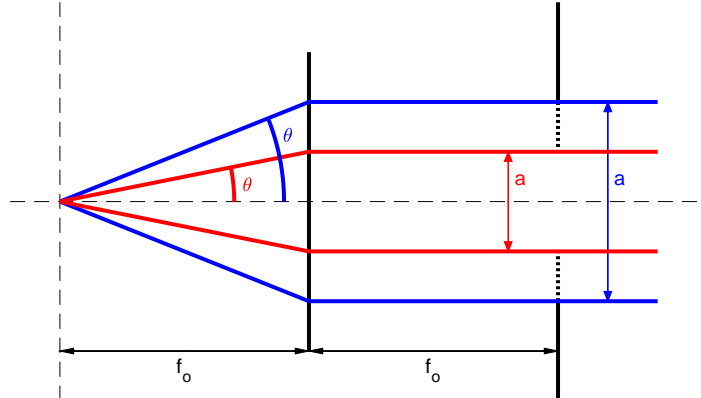


Figure 2.2: Aperture geometry.

Where λ is the wavelength of light and Δxy is the distance in the image plane which can be resolved (i.e. the pixel size of the camera). In imaging of transparent samples (e.g. tissues) it is often desirable to have a small DOF to sharply resolve a single layer in the sample. In imaging of opaque objects, such as the regoliths in this thesis, it can instead be desired to have a large DOF to capture the entire object in focus.

The relative sizes of the aperture a and the diameters of the lenses a_o and a_t limit the maximum field of view h which may be imaged by:

$$h \leq \frac{a_o - a}{2} \quad \text{and} \quad h \leq \frac{d}{f_o} \cdot \frac{a_f - a}{2} \quad (2.4)$$

2.2 Light field microscopy

Light from a sample can be fully characterised by a four dimensional function: the light field [Levoy and Hanrahan, 1996]. This function contains information of the position as well as the propagation direction of the light rays. In a light field camera or microscope, the goal is to capture this information. In a typical microscope positions are discretised into pixels representing a point (x, y) in the sample. In a light field microscope the light ray from a point (x, y) is also characterised by the point (u, v) it passes through the aperture as shown in Figure 2.3. A light ray is thus described by the four dimensional value (x, y, u, v) .

Light field microscopy can be realised by two optically simple methods, shown in Figure 2.4. In the programmable aperture microscope the aperture positions (u, v) are either imaged sequentially, or multiplexed and computationally separated, see [Liang et al., 2008], to reduce the number of images

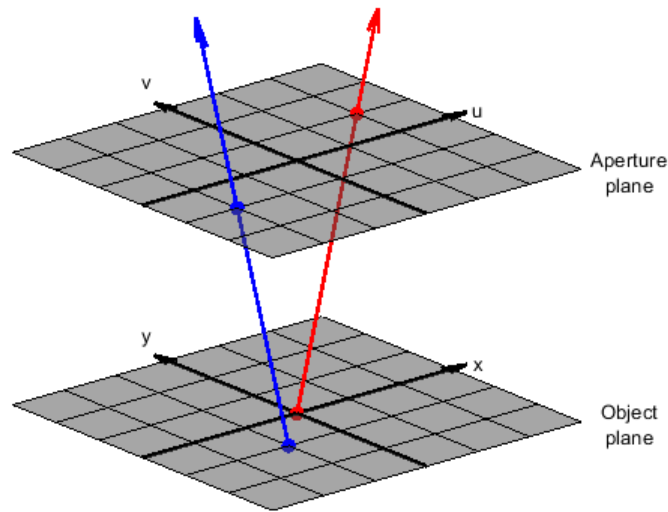


Figure 2.3: Light rays are uniquely defined by their intersections (x, y) and (u, v) with two planes. The geometry here is simplified; the objective lens will refract these rays before reaching the aperture plane.

required. The microlens array microscope captures the four dimension of (x, y, u, v) simultaneously. However, resolution in (x, y) is traded away for resolution in (u, v) , with the product of the two limited by the number of pixels on the camera sensor. For example, if a 1000×1000 pixel sensor is used with a 200×200 microlens array the resolution in (u, v) is 5×5 , and the resolution in (x, y) is 200×200 . The best choice of technique depends on the application. In the SPEARS microscope we are imaging static objects, and thus choose to use a programmable aperture microscope to maximise the resolution. The aperture is realised with a transparent LCD, demonstrated in Figure 2.5.

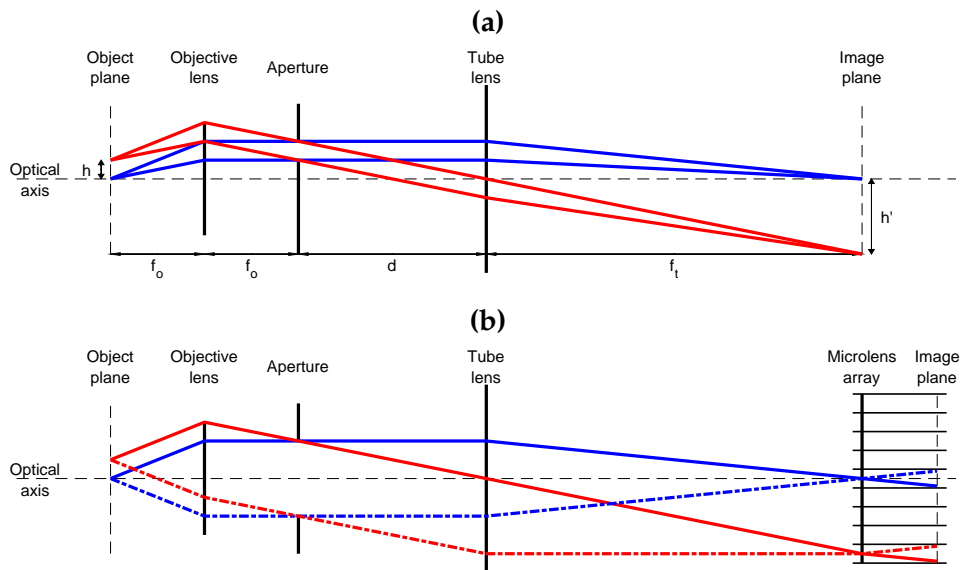


Figure 2.4: Two types of light field microscopes. **(a)** shows a programmable aperture microscope. (u, v) is dictated by the position of the aperture, and all of (x, y) is imaged with the camera sensor. **(b)** shows a microlens array microscope. The camera sensor is compartmentalised by a microlens array. The (x, y) position is encoded by which microlens the ray passes through and the aperture position (u, v) is encoded by the pixel struck on the sensor.

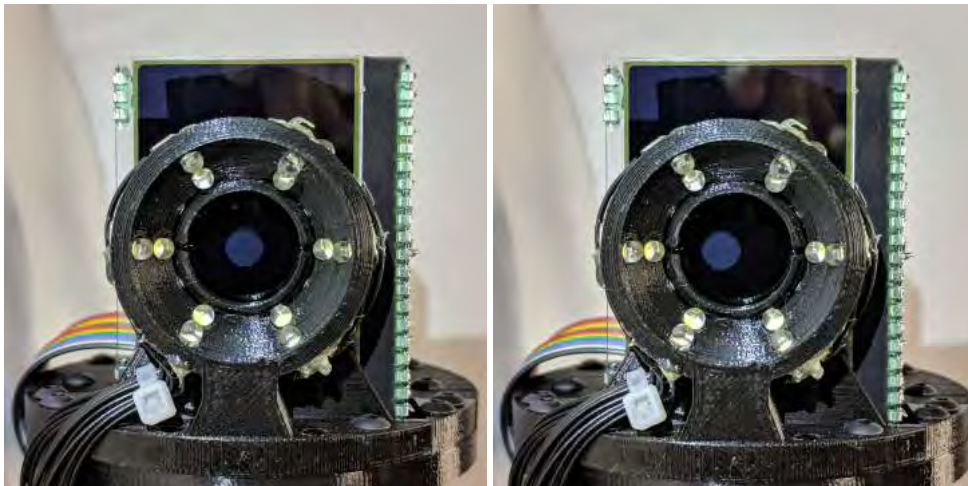


Figure 2.5: The programmable LCD aperture in the miniaturised (Chapter 6) microscope. Left: Centered, Right: Offset. The objective lens has been removed to show the aperture.

2.3 Controlled illumination microscopy

An additional source of 3D information is controlled illumination microscopy (CIM) where the sample is illuminated from several point sources in sequence. Since the light is from a distinct and known direction, the sizes and shapes of shadows and highlights correspond to the shape of the object. Shape-from-shading is a family of methods to infer the shape based on images with known lighting. A single light source (e.g. the Sun) can be used for this purpose, which is commonly applied to recover 3D data from satellite images, e.g. [Kirk et al., 2003]. In this work, we use many light sources in a CIM setup and apply the shape-from-shading method of photometric stereo [Woodham, 1980] to infer shape. Figure 2.6 shows an example of CIM data. The critical design parameter for CIM is the placement and number of light sources applied. Fundamentally, there is a trade-off between higher obtainable resolution with closely spaced lights, and the linearly increasing capture time and data volume. Recently these methods have been extended to continuously variable illumination which provides faster high resolution normal map data [Francken et al., 2008].

2.3.1 Contrast and specularity enhancement

The data from CIM can be directly used to enhance the viewing of the sample. In traditional imaging, the sample is flood-lit with all available light sources enabled. This is equivalent to constructing the pixel-by-pixel average across the light sources in the CIM dataset. An alternative approach is to construct the pixel-by-pixel maximum value across the CIM dataset. This enhances the brightness of the parts of the scene which are illuminated by only one or a few of the light sources and emphasises specular regions. A comparison is shown in Figure 2.7.

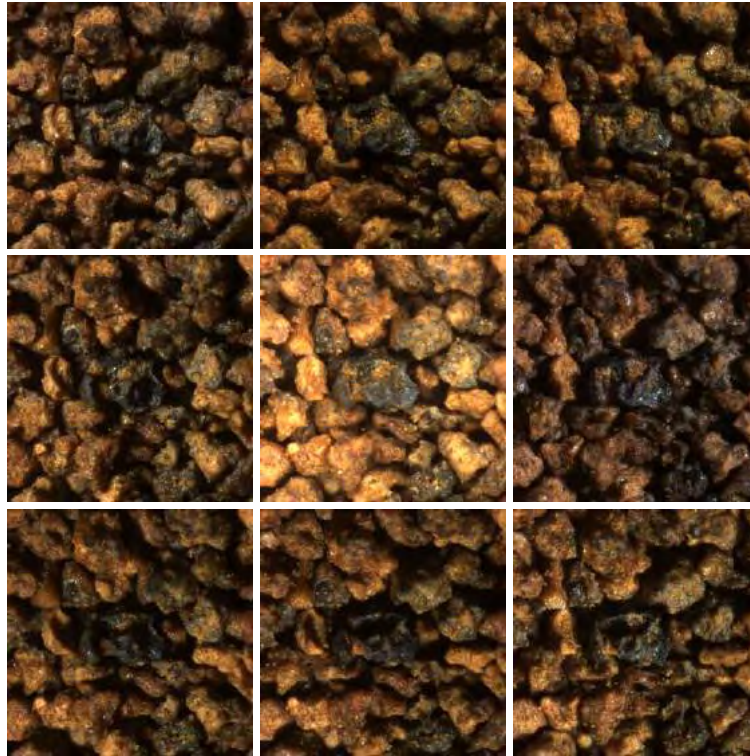


Figure 2.6: CIM data for eight light sources. In the centre image all lights are on. In the surrounding images a single light source from the respective direction is on. (Top image is illuminated from the top and so forth.)

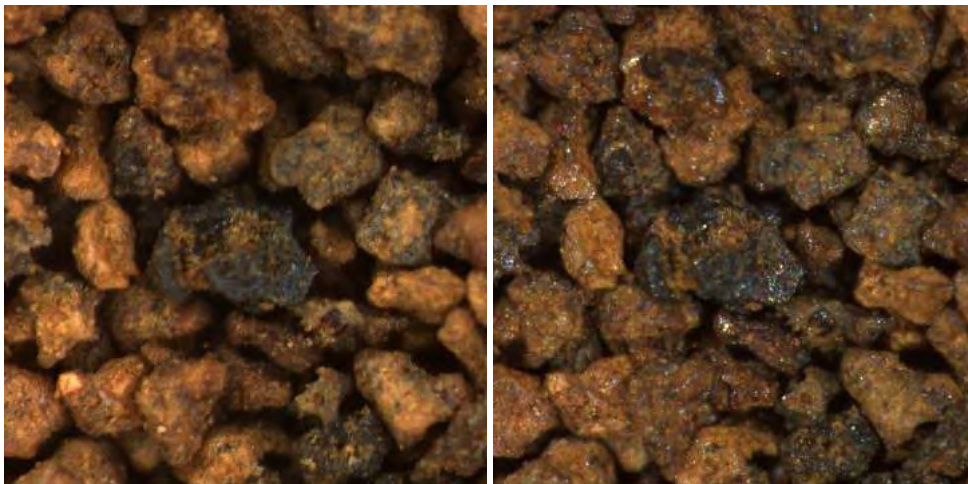


Figure 2.7: Comparison between standard flood-lit and CIM enhanced images. Left: All lights enabled. Right: Maximum-intensity projection across all light sources.

3 SPEARS demonstrator microscope

3.1 Optical table setup

We built a bench-top demonstrator microscope to show proof-of-concept and capture most of the data in this work. In Chapter 6 we present an optically similar miniaturised version of this system. The microscope is shown in Figures 3.1–3.3. Its components are:

1. Allied Vision Technologies (AVT) Manta G-146C 1/2" CCD camera (1360 × 1024 pixels, 4.65 μm each, 12-bit ADC).
2. Fujinon HF75HA-1B tube lens ($f_t = 75$ mm, $a_t = 27$ mm).

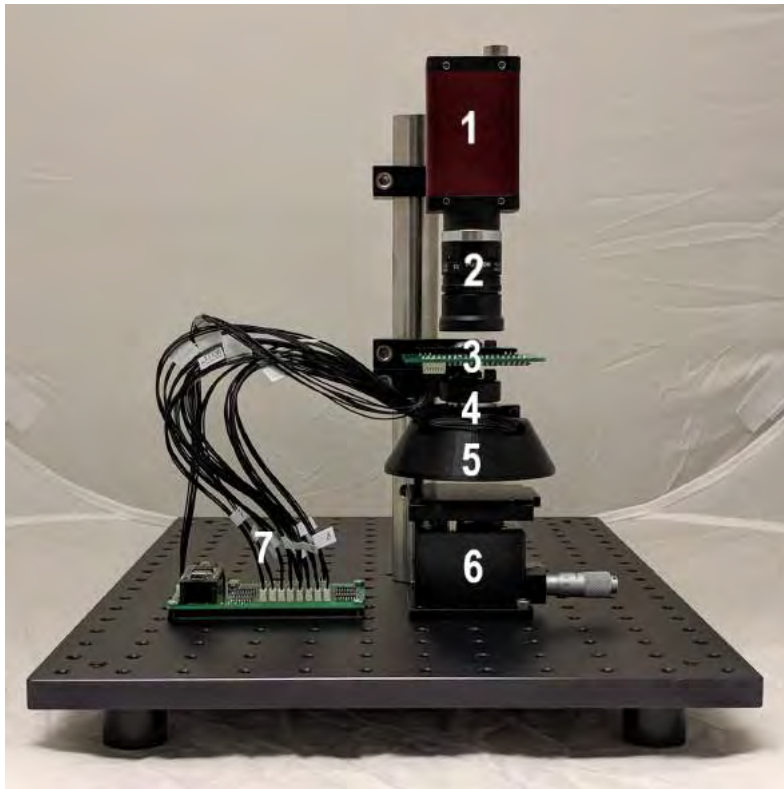


Figure 3.1: The SPEARS demonstrator microscope.

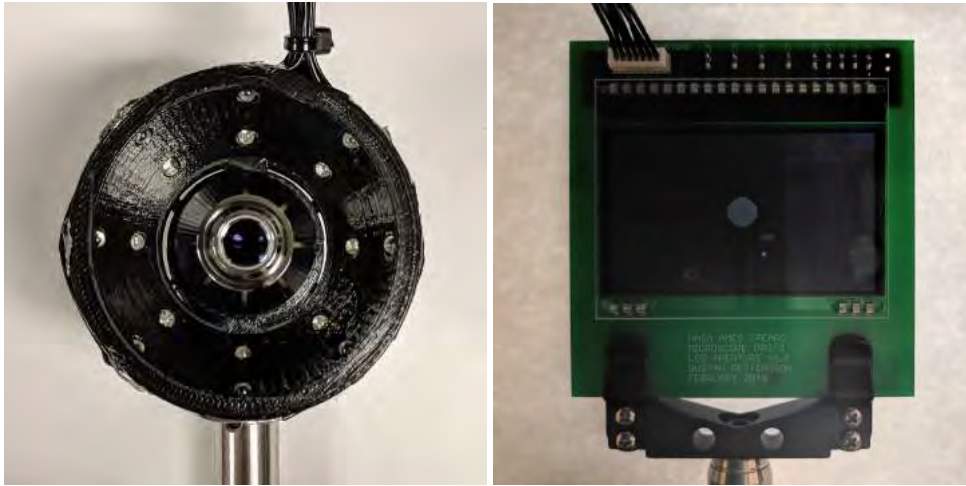


Figure 3.2: Left: View inside the objective and LED dome. Right: The LCD aperture PCB showing a central aperture.



Figure 3.3: Control electronics for the microscope.

3. Electronic Assembly DOGM128S-6 transparent LDC (128×64 pixels, $.36 \times .42$ mm each), mounted on a PCB.
4. Olympus Plan Acromat 10x/NA .25 objective ($f_o = 18$ mm, $a_o = 9$ mm), inside the dome as seen in Figure 3.2.
5. 16 Vishay Semiconductor VLHW4100 white 3 mm LEDs (inside dome).
6. Edmunds Optics (EO) z-axis stage (60×60 mm² platform).
7. Control electronics PCB with Teensy 3.2 microcontroller and 48 channel LED driver, see Figure 3.3.

The magnification of the system is $M = 75/18 = 4.17$, leading to a pixel size in the object plane of $4.65 \mu\text{m}/4.17 = 1.12 \mu\text{m}$. We record the centre 1000×1000 pixels and thus produce an image field which is 1.12 mm wide. This was confirmed by imaging a calibration scale.

The sample is illuminated by a set of 16 LEDs mounted in a 3D-printed dome shown in Figure 3.2. The LED positions approximate a hemisphere around the sample with two rows at an elevation of 22.5° and 45° respectively. The latter angle is close to the maximum elevation possible without obstruction from the objective, whereas the former was chosen to allow the dome to stand 8 mm clear of the sample and thus image uneven objects. The LCD pixels and the LEDs are individually controlled by electronics based on a Teensy 3.2 microcontroller and a set of 48 constant-current drivers. The schematics and PCB design are shown in Appendix B.

3.2 Light field microscopy in practice

The resolution in (u, v) of this setup is limited by the contrast of the LCD. When the LCD is commanded to be closed, some light leaks through. With small apertures the leakage through the closed section of the LCD dominates the image. To combat this two images are captured: One image when the aperture is set to the desired diameter and one background image when the aperture is fully closed. By subtracting the background image, the leakage is removed as demonstrated in Figure 3.4. This process limits the usable range of the camera from its native (12-bit or 4096 values) since a part of this range is used by the background image. If the relative mean intensity for an aperture size compared to the background is I , the usable fraction is: $c = (I - 1)/I$. The measurements in Figure 3.5 show I for a series of small apertures. The smallest usable aperture is 1.5 mm where $I = 1.3 \Rightarrow c = .23$; losing circa two bits of depth.

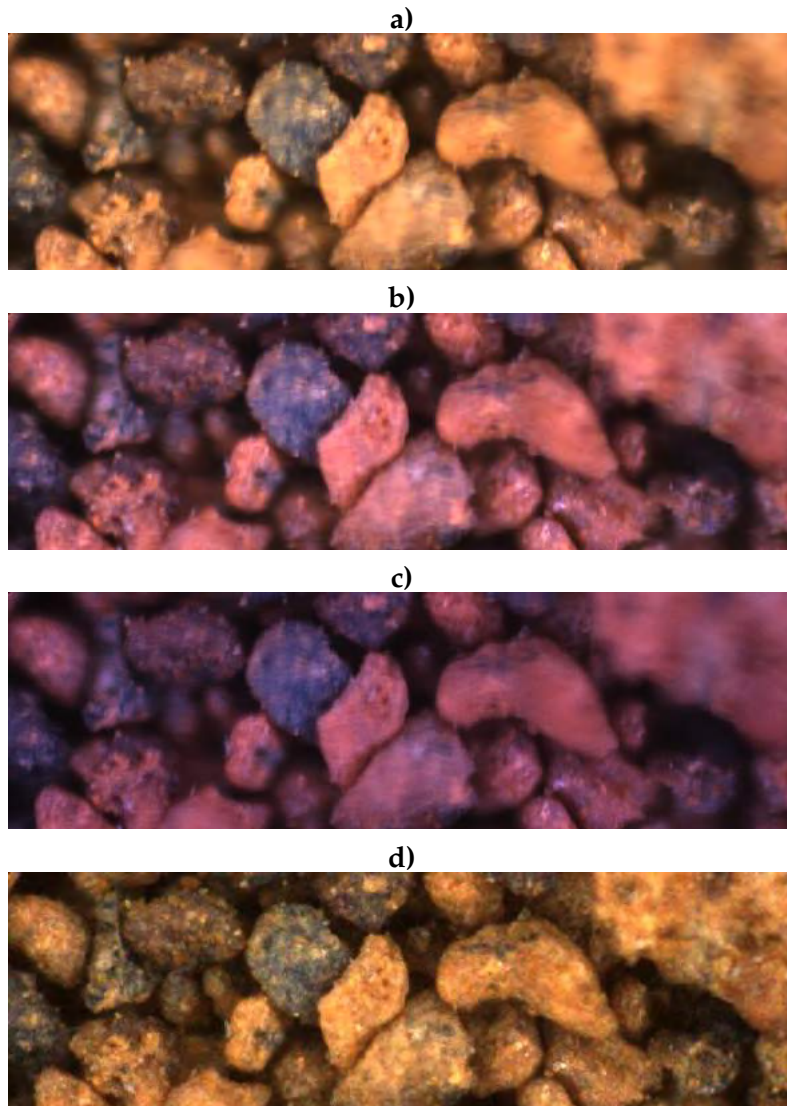


Figure 3.4: Comparison of aperture sizes. **a)** Fully open aperture, 20 ms exposure. **b)** Small (1.5 mm) aperture, 100 ms exposure. **c)** Fully closed aperture, 100 ms exposure. **d)** Image b) minus image c), scaled by 4. Notice that the DOF in d) is greater than in a), and that the small aperture b) and closed aperture c) are similar due to the limited LCD contrast.

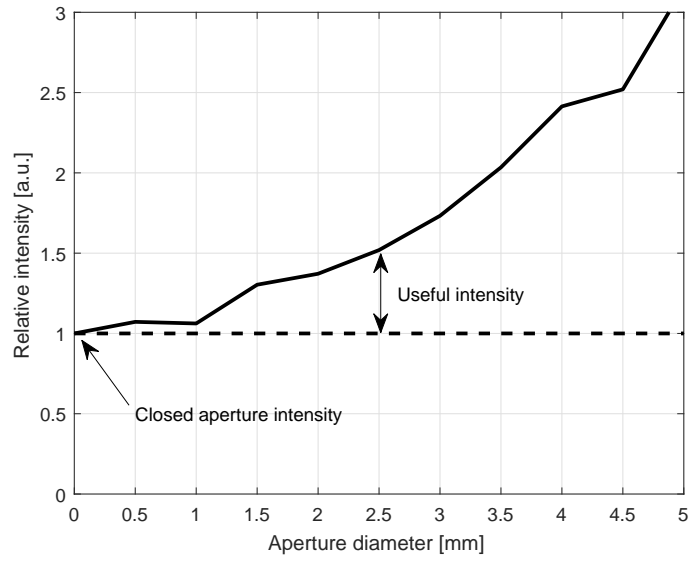


Figure 3.5: Measurement of the (LCD) aperture contrast. The steps in the curve are likely due to the pixel size (≈ 0.4 mm) quantising the aperture.

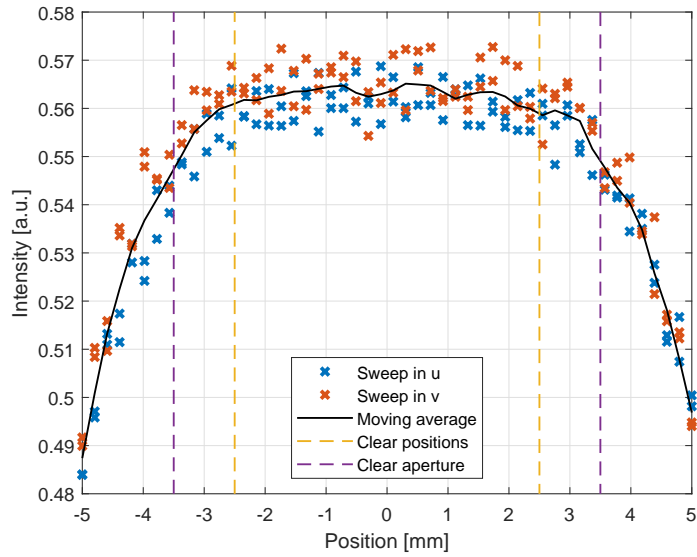


Figure 3.6: Measurement of the alignment and size of the aperture. A circular 2 mm diameter aperture was moved across the LCD in the horizontal (u) and vertical (v) direction. The measurements are centred about zero (showing proper alignment) and the intensity falls off at ± 2.5 mm implying a measured clear aperture of the system of $a = 5 + 2 = 7$ mm.

The objective used in the setup is designed for microscopy. Thus there is a physical aperture placed one focal length behind the lens to achieve telecentricity, as discussed in Section 2.1. Therefore it is only possible to place the LCD aperture farther back from the objective lens. Stepping slightly away from telecentricity is not critical in this application. However the usable aperture at the LCD will be smaller than the specified $a = 9$ mm of the objective. The exact effects are beyond the scope of this thesis, and we will approximate the system as telecentric. The usable size of the aperture at the LCD is measured by sweeping a small aperture across the LCD in Figure 3.6. The intensity falls off (the image is vignetted) when the aperture is moved outside the usable range. We measure a useful aperture of $a = 7$ mm.

Once the smallest usable aperture and the total useful aperture of the system is determined an aperture position sequence is created. It is desirable to have as many apertures as possible for better resolution in u, v . The apertures are arranged in a hexagonal pattern for optimal packing. The two highest density aperture patterns possible are shown in Figure 3.7.

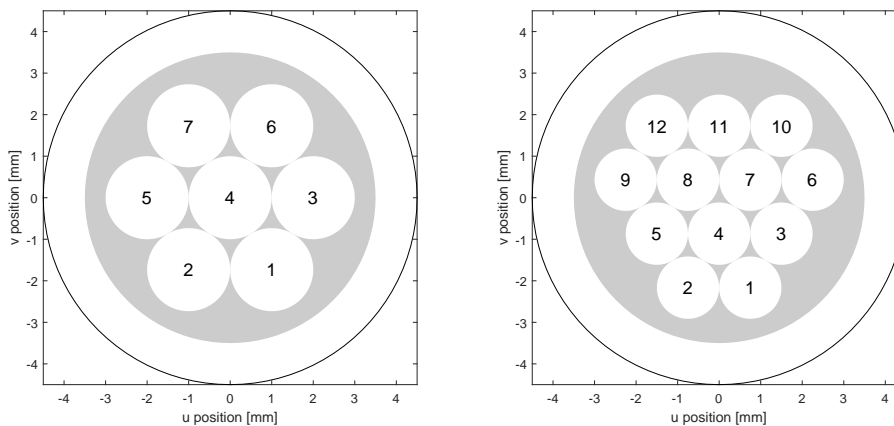


Figure 3.7: Two possible circular aperture patterns. Left: 7 apertures, 2 mm each (7×2 mm). Right: 12 apertures, 1.5 mm each (12×1.5 mm). The large circle is the 9 mm aperture of the objective, the gray disk is the useful $a = 7$ mm aperture at the LCD.

4 Shape reconstruction

4.1 Light field to surface height

There are several existing algorithms which may be applied to the light field images, with the classic example being to artificially shift the focal plane [Ng et al., 2005]. In this work, we focus on reconstructing the depth (or height) of the imaged object. A common method for this is to first apply a focal-shifting algorithm, followed by a focus-to-depth algorithm. It has been shown that this is mathematically equivalent to directly applying a (multi-view) stereo-disparity algorithm to the images [Schechner and Kiryati, 2000], where the shift in the position of an object between the images is calculated. In this section, we apply a stereo-disparity algorithm with a pyramid filter and show that it reliably reproduces height maps.

4.1.1 Disparity correlation

The disparity between two images A and B is a measurement on a block-by-block (say 8×8 pixels) basis, describing how far a block from image A needs to be moved to be aligned with the same object in image B . The disparity is found by placing the block from image A on top of image B , first in its original position. The difference between the block of image A and image B below is measured by a correlation score (usually the mean absolute difference, or mean square difference between each pixel in the block). Then, the block from A is shifted by one pixel and the correlation calculated again. The pixel-shift with the lowest correlation score is the disparity. Figure 4.1 shows the process for two images of JSC Mars-1 [U. of Central Florida] simulant. The individual grains can be discerned in the disparity and noise is visible; some blocks differ significantly from their neighbours. Using larger blocks will reduce the noise but also decrease the resolution. To reduce computation time the correlation is not computed sequentially for each block. Instead, the entire A image is translated across B , and the pixel-by-pixel correlation score is recorded. Averaging the pixel-by-pixel correlation into the desired block size, and finding the minimum afterwards, is mathematically equivalent to the block-wise minimisation. Additionally, considerable flexibility is added by choosing the block-size after the fact.

In light field microscopy and multi-view stereo alike, there are more than two images available. In our case, with seven images there are 21 pairs, and

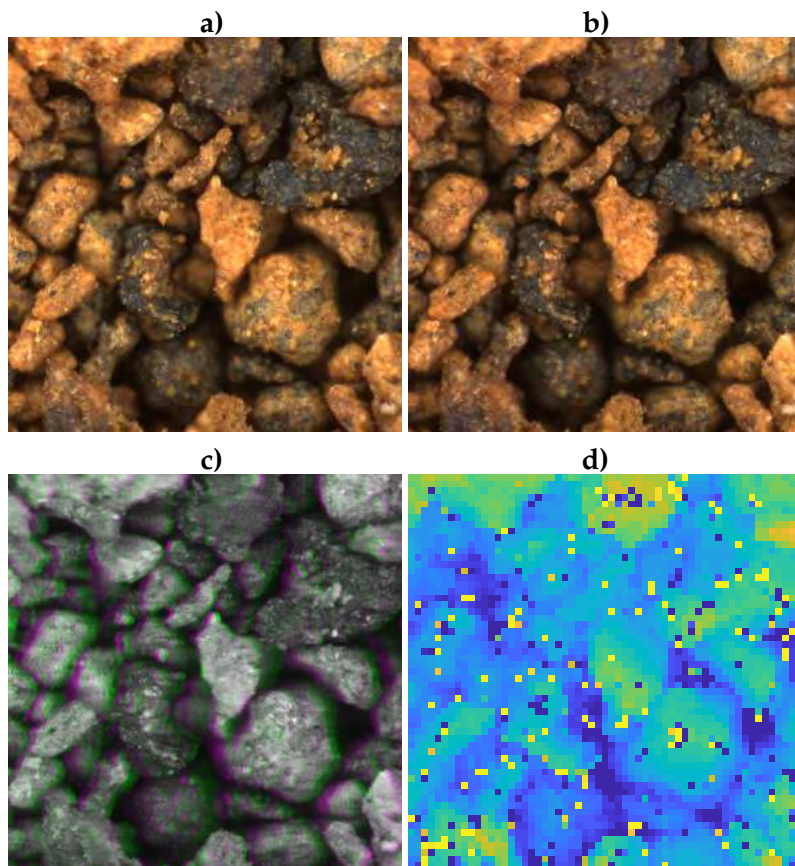


Figure 4.1: Stereo images and disparity. **a)** and **b)** show the 1000×1000 pixel left and right image respectively of a sample. **c)** shows the left and right images in a green and magenta composite. **d)** shows the disparity calculated for 16×16 pixel blocks. Blue blocks have negative disparity and yellow blocks have positive disparity.

with 12 images there are 66 pairs for which the disparity can be calculated with. By correlating disparity across several image pairs, the resolution and noise are both improved. In these images the disparity is not only in the left-right direction so a 2D translation is required where the images are moved in accordance to the direction they were captured from. In multi-camera stereo systems these positions may need to be calibrated to reliably reconstruct the depth. In our microscopy system however, these are well defined due to using a single camera and a programmable aperture, removing the need for calibration. Consider for this discussion the seven aperture pattern in Figure 3.7 left. The positions of each aperture, normalised to one aperture diameter, are:

i	1	2	3	4	5	6	7
u_i	.5	-.5	1	0	-1	.5	-.5
v_i	-.866	-.866	0	0	0	.866	.866

Let $\mathbf{p}_i = [u_i, v_i]^T$ be the vector from the origin to the centre of aperture i . The image taken with aperture i must then be translated in the \mathbf{p}_i direction in the xy plane¹ for features that are closer to the camera than the object plane to align with the centre image. In general, any two images may be correlated. In this case both images are translated with their respective \mathbf{p}_i . This guarantees that the correlation scores produced by two offset images are related to the object position in the centre image. For the seven aperture case the possible aperture pairs are given below:

n	1	2	3	4	5	6	7	8	9	10	11
s_n	1	1	1	1	1	1	2	2	2	2	2
t_n	2	3	4	5	6	7	3	4	5	6	7

n	12	13	14	15	16	17	18	19	20	21
s_n	3	3	3	3	4	4	4	5	5	6
t_n	4	5	6	7	5	6	7	6	7	7

The correlation score is calculated for each pair (s_n, t_n) on a pixel-by-pixel basis. The images are converted to 8-bit grayscale before the algorithm is started. Let the number of pairs be N , and let d be the translation distance (in pixels) to be trialed. Assuming $\text{IMG}(s)$ refers to the image from aperture s and a function imTrans exists to translate the image the score is: (the x, y indices are the image pixels)

$$c_{x,y,d,n} = |\text{imTrans}(\text{IMG}(s_n), \mathbf{p}_{s_n} \cdot d) - \text{imTrans}(\text{IMG}(t_n), \mathbf{p}_{t_n} \cdot d)| \quad (4.1)$$

¹In our coordinates positive y is up and positive x is to the right.

This four dimensional correlation score is calculated for every pair n and a range of translations d (e.g. from -35 to 35 pixels). This data needs to be consolidated into a two dimensional disparity with one value for each pixel. First, the score across all image pairs n is averaged:

$$c_{x,y,d} = \frac{1}{N} \sum_{n=1}^N c_{x,y,d,n} \quad (4.2)$$

Following this, the score may be averaged to a desired block size, reducing the size in the x, y dimensions. The disparity $D_{x,y}$ is then found by minimising:

$$D_{x,y} = \min_d c_{x,y,d} \quad (4.3)$$

Figure 4.2 shows the correlation for a number of block sizes and compares the multi-pair results to using a single stereo pair. The reconstruction is improved and meaningful data is produced on the pixel-by-pixel level.

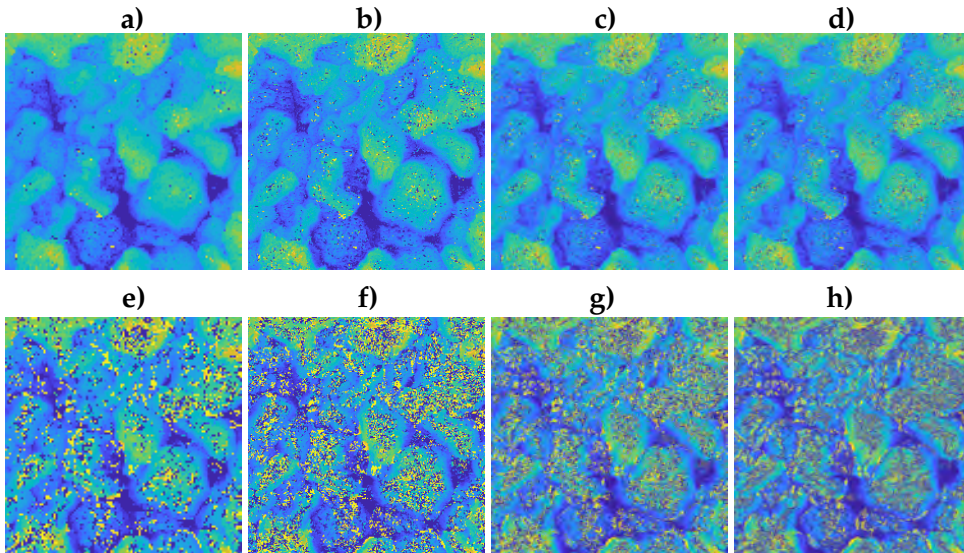


Figure 4.2: Comparison of block sizes and single vs. multiple pairs. **a)-d)** show the correlation done for all 21 pairs, in block sizes of 8, 4, 2, and 1. **e)-h)** show the correlation done for only one pair (the left-right (5, 3) pair), in block sizes of 8, 4, 2, and 1. The scene is the same as in Figure 4.1.

4.1.2 Pyramid filtering of disparity

As previously discussed, there is a trade-off in choosing block size for calculating the disparity. A smaller block size recovers more details in the disparity but is noisier. To remove this noise the output must be filtered. Simple filters

such as median filtering or Gaussian blurring can be effective in removing the noise, however, some detail is always lost. This is especially a problem for large transitions in disparity at the edges of objects. Since we have several block-size disparity maps available at low computational cost,² we wish to use a filter which keeps the details from small block sizes where available, but falls back to the larger blocks where noise is present. To do this we will apply a pyramid processing method, see [Bovik, 2009, chapter 6], gradually refining the disparity map from large to small blocks, and filtering out the noise in each step. Start with a large block-size disparity map, $F_{x,y}$, with block-size 2^k , and follow this process:

1. Calculate the 2^{k-1} block-size disparity map $D_{x,y}(k-1)$ and upscale $F_{x,y}$ to twice the resolution in x and y .
2. Find the difference in each pixel: $\Delta_{x,y} = |D_{x,y}(k-1) - F_{x,y}|$.
3. If $\Delta_{x,y}$ is smaller than some threshold (e.g. 2^k), update the map $F_{x,y}$ with the refined disparity, otherwise reject the refined disparity as noise:
$$F_{x,y} = \begin{cases} D_{x,y}(k-1), & \text{if } \Delta_{x,y} < 2^k \\ F_{x,y}, & \text{otherwise} \end{cases} .$$
4. Filter $F_{x,y}$ with a 3×3 median filter.
5. If $k > 0$, set $k = k - 1$ and return to step 1. Else stop.

Thresholding by the difference from the previous block-size rejects most of the noise present in the smaller block disparity map. Any remaining noise has been bounded by this process to be on the order of the block size, and is thus removed by applying a weak filtering. Figure 4.3 shows how the disparity map is gradually refined to the pixel level while rejecting noise. Sharp transitions in disparity are preserved well in this process. One should not be misled that the height map in Figure 4.3h is true to life down to the pixel level. The pitting seen is not real, but noise in the reconstruction which this method does not reject.

²Almost all computational time is spent calculating Eq. (4.1). The subsequent block-averaging and minimisation are fast processes.

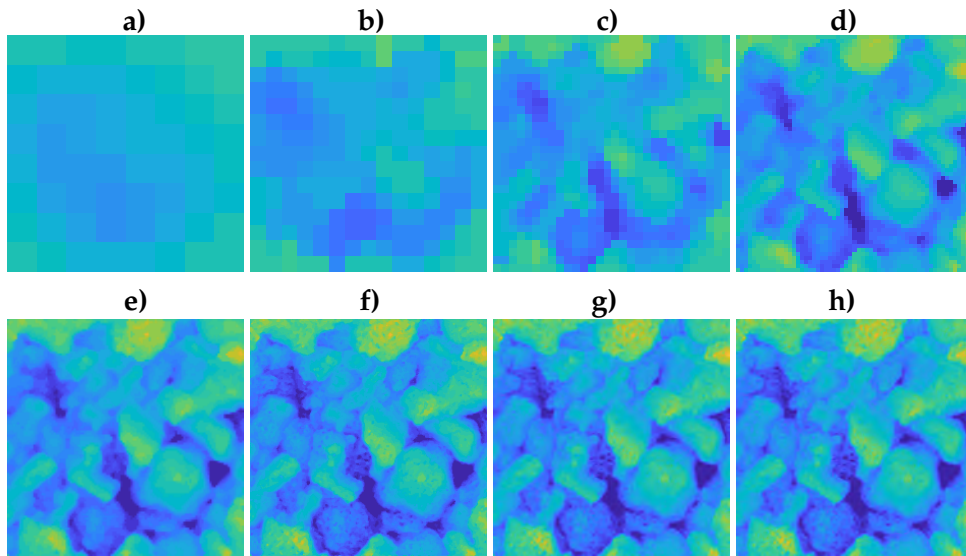


Figure 4.3: Evolution of disparity through pyramid filtering. **a)-h)** show a pyramid filter starting with $2^7 = 128$ block-size and ending at $2^0 = 1$ block-size. The same 21 aperture pairs data as in Figure 4.2a–d is used.

4.1.3 Disparity to physical height

Figure 4.4 shows how objects offset from the object plane are imaged. If the aperture is centered each object will be imaged as if it was in the object plane (possibly out of focus) since the system is telecentric. When the aperture is offset by a distance p from the optical axis the objects outside the object plane will appear to shift a distance d , the disparity. By similar right triangles the height of an object h is linked to the disparity d by:

$$\frac{h}{d} = \frac{f_o}{p} \quad (4.4)$$

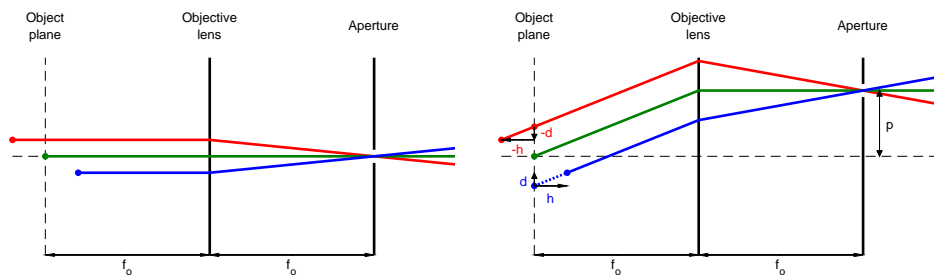


Figure 4.4: Geometry linking disparity d to height h in a sample.

In this expression, h will be given in pixels. By multiplying with the pixel size in object space (i.e. $1.12 \mu\text{m}$ for the bench prototype) the physical size is recovered. For the bench microscope and the ($7 \times 2 \text{ mm}$) aperture pattern this factor becomes:

$$\frac{h}{d} = \frac{18 \text{ mm}}{2 \text{ mm}} \cdot 1.12 \mu\text{m}/\text{px} = 10.0 \mu\text{m}/\text{px} \quad (4.5)$$

If the preferred $12 \times 1.5 \text{ mm}$ aperture pattern is used this instead becomes $13.4 \mu\text{m}/\text{px}$. In Figure 4.5 this value is calibrated by moving a sample vertically with a micrometer linear stage. The measured value ($14.9 \mu\text{m}/\text{px}$ or $h/d = 13.3$) agrees well with theory, and the measurement also shows that zero disparity is aligned with the centre of the focal plane as expected.

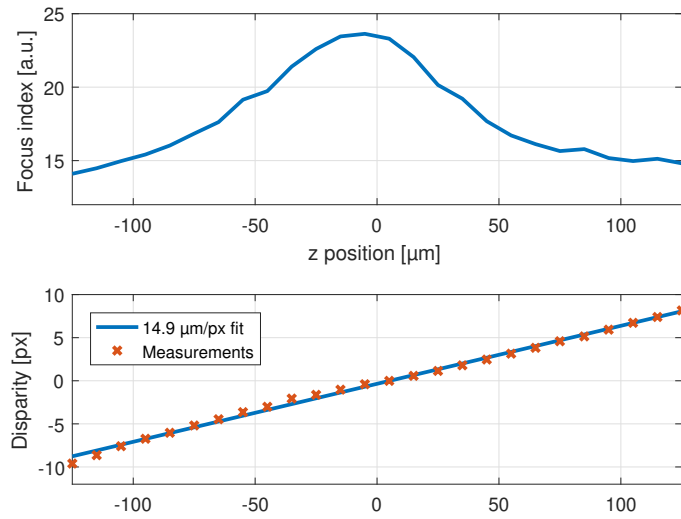


Figure 4.5: DOF measurement and calibration of disparity for $12 \times 1.5 \text{ mm}$ aperture pattern. A sample is moved in known steps of $10 \mu\text{m}$ and the focus index and disparity is recorded. The height to disparity factor is measured to $14.9 \mu\text{m}/\text{px}$ or $13.3 \text{ px}/\text{px}$.

4.2 Controlled illumination to surface normal

Using a large number of known light sources the normal vectors of the sample can be recovered based on a model of the reflection from the sample. A simple reflectance model is the Lambertian model [Wong, 2012, chapter 5] where the intensity depends only on the cosine of the angle between the illumination and surface normal. The geometry is shown in Figure 4.6. For a

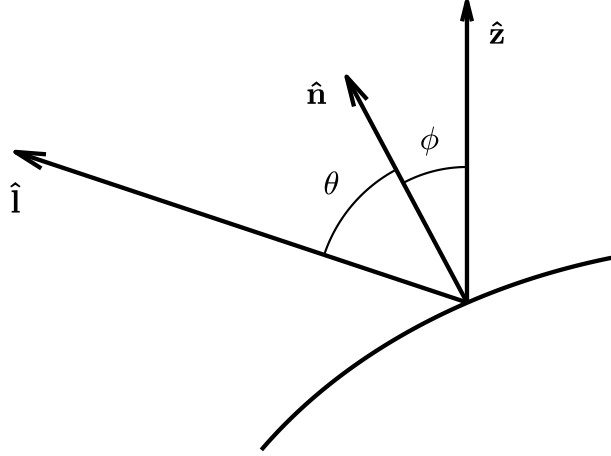


Figure 4.6: Geometry showing a surface normal and light source direction. In the microscope the scene is always observed from the \hat{z} direction.

light source coming from a direction \hat{l} , and striking a surface with normal \hat{n} , the intensity (observed from any direction) is:

$$i = \rho \hat{l} \cdot \hat{n} = \rho \hat{l}^T \hat{n} \quad (4.6)$$

Where ρ is a scalar containing the intensity of the light source and the surface albedo. If this is absorbed into the normal vector, $\mathbf{n} = \rho \hat{n}$, and the scene is observed using m unique light sources with directions $\mathbf{L} = [\hat{l}_1, \hat{l}_2, \dots, \hat{l}_m]$, measuring the intensities $\mathbf{i} = [i_1, i_2, \dots, i_m]$, the following system of equations must hold:

$$i_1 = \tilde{\mathbf{l}}_1^T \mathbf{n} \quad i_2 = \tilde{\mathbf{l}}_2^T \mathbf{n} \quad \dots \quad i_m = \tilde{\mathbf{l}}_m^T \mathbf{n} \quad (4.7)$$

or in matrix form:

$$\mathbf{i} = \mathbf{L}^T \mathbf{n} \quad (4.8)$$

Assuming $m > 3$ this system is over-determined and can be solved for \mathbf{n} in a least squares sense with the normal equations:

$$\mathbf{n} = (\mathbf{L}\mathbf{L}^T)^{-1} \mathbf{L}\mathbf{i} \quad (4.9)$$

This equation is extended to solve for every pixel in the images at once (assuming P pixels) by appending:

$$\mathbf{N} = [\mathbf{n}_1, \mathbf{n}_2, \dots, \mathbf{n}_P] \quad (4.10)$$

$$\mathbf{I} = [i_1, i_2, \dots, i_P]^T \quad (4.11)$$

and solving by:

$$\mathbf{N} = (\mathbf{L}\mathbf{L}^T)^{-1}\mathbf{L}\mathbf{I} \quad (4.12)$$

The magnitude of the resulting normal vector field \mathbf{N} is the albedo ρ for each pixel. This is saved and the vector field is normalised into \mathbf{N}^m . Figure 4.7 shows an example of the output.

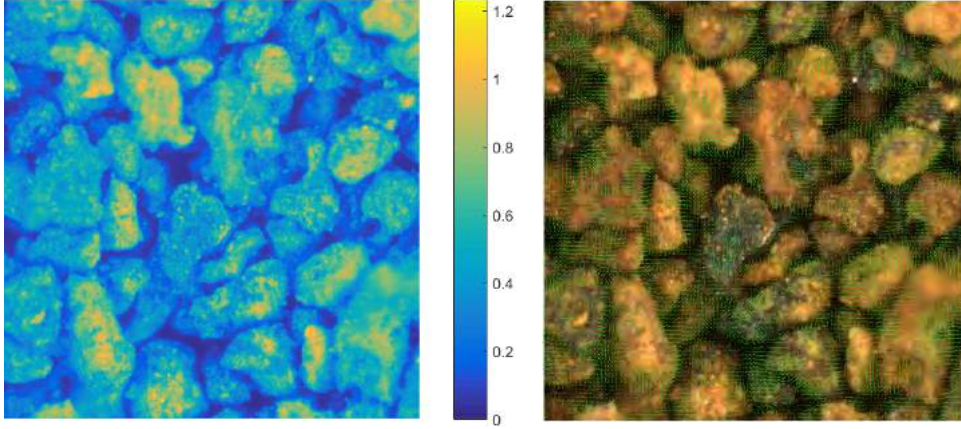


Figure 4.7: Left: magnitude ρ from reconstruction. Right: x and y components of normal vectors overlaid on a colour 2D image. Every tenth vector is shown and no smoothing has been applied.

4.3 Combining disparity and normals

We have two independent measurements of the same 3D surface \mathbf{Z} . Multi-view stereo which measures the surface \mathbf{Z}^m , and photometric stereo which measures the normal vector field \mathbf{N}^m . We use the superscript m to indicate a measurement. Ideally, these two measurements match precisely the true surface, i.e. $\mathbf{Z}^m = \mathbf{Z}$, and:

$$\mathbf{N}^m = \left[-\frac{\partial \mathbf{Z}}{\partial x}, -\frac{\partial \mathbf{Z}}{\partial y}, 1 \right]^T \bigg/ \sqrt{\frac{\partial \mathbf{Z}^2}{\partial x} + \frac{\partial \mathbf{Z}^2}{\partial y} + 1} \quad (4.13)$$

We observe that this does not hold because the disparity measurement contains high frequency noise, and the normal vector field has a low frequency bias.

We adapt the method of [Nehab et al., 2005] to telecentric geometry and correct our estimates of both \mathbf{N} and \mathbf{Z} . There are two steps: 1) Correct the measured normals \mathbf{N}^m by replacing their biased low-frequency component with a reliable low-frequency component calculated from \mathbf{Z}^m . Call this

\mathbf{N}^c . 2) Correct the measured height-map \mathbf{Z}^m by finding a surface \mathbf{Z}^c which minimizes the error to both \mathbf{Z}^m and \mathbf{N}^c according to Eq. (4.13).

4.3.1 Correcting normals

Let \mathbf{N}^m be the measured normals using photometric stereo as before, and let \mathbf{N}^p be the normals computed using \mathbf{Z}^m . Find each component of \mathbf{N}^p by:

$$\mathbf{N}_x^p = -\frac{1}{8}\mathbf{Z}^m * \begin{bmatrix} -1 & 0 & 1 \\ -2 & 0 & 2 \\ -1 & 0 & 1 \end{bmatrix} \quad (4.14)$$

$$\mathbf{N}_y^p = -\frac{1}{8}\mathbf{Z}^m * \begin{bmatrix} 1 & 2 & 1 \\ 0 & 0 & 0 \\ -1 & -2 & -1 \end{bmatrix} \quad (4.15)$$

$$\mathbf{N}_z^p = 1 \quad (4.16)$$

and then normalising. Here $*$ denotes convolution and the matrices are the Sobel-Feldman [Sobel, 2014] approximations to $\partial/\partial x$ and $\partial/\partial y$ respectively. Let the operator $S(\cdot)$ smooth the normals by applying coordinate-wise Gaussian filtering with standard deviation σ and renormalising. Then, find the rotation field \mathbf{R} which recovers the high-frequency part of \mathbf{N}^m by rotating the smoothed normals in $S(\mathbf{N}^m)$ onto the original \mathbf{N}^m : $\mathbf{N}^m = \mathbf{R}S(\mathbf{N}^m)$. By applying this rotation field to $S(\mathbf{N}^p)$ the high-frequency component of \mathbf{N}^m is combined with the low frequency component of \mathbf{N}^p , giving the corrected normal by: $\mathbf{N}^c = \mathbf{R}S(\mathbf{N}^p)$. Figure 4.8 shows an example of the process. The standard deviation of the Gaussian filter in $S(\cdot)$ decides the frequency cut-off. Using $\sigma = 15$ pixels yields good results.

4.3.2 Correcting disparity

Our goal is to find a surface \mathbf{Z}^c which represents some best fit to both the corrected normals and the measured height-field. This is formulated as a linear-least-squares optimization problem where the errors in normals and positions are weighted together. Stack every column of \mathbf{Z}^m atop each other such that it has the dimension $P \times 1$ (call this \mathbf{z}^c) and separate out the components of \mathbf{N}^c into $\mathbf{n}_x^c, \mathbf{n}_y^c$ after normalising such that $\mathbf{N}_z^c = 1$ (allowing the root to be dropped from Eq. (4.13)). Now consider the following three equations:

$$\mathbf{I}\mathbf{z} = \mathbf{z}_m \quad (4.17)$$

$$\mathbf{T}_x\mathbf{z} = -\mathbf{n}_x^c \quad (4.18)$$

$$\mathbf{T}_y\mathbf{z} = -\mathbf{n}_y^c \quad (4.19)$$

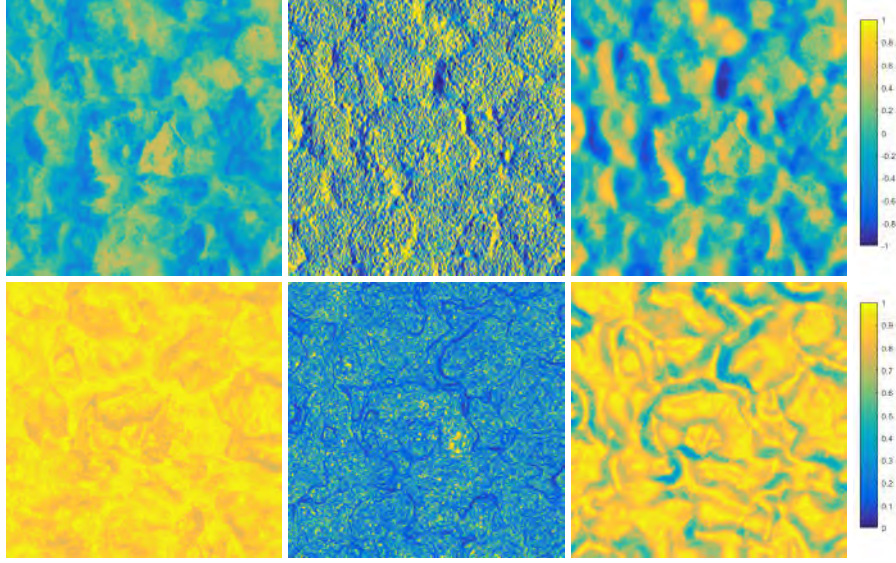


Figure 4.8: Top row, left to right: x -component of \mathbf{N}^m , \mathbf{N}^p , and \mathbf{N}^c . Bottom row, left to right: z -component of \mathbf{N}^m , \mathbf{N}^p , and \mathbf{N}^c .

Here, \mathbf{I} is the $P \times P$ identity matrix, and \mathbf{T}_x and \mathbf{T}_y are $P \times P$ matrices which when multiplied with \mathbf{z} produce a finite difference approximation of the derivatives $\partial z / \partial x$ and $\partial z / \partial y$ respectively. The Sobel operators from Eqs. (4.14)–(4.15) are used again.³ Assuming the matrices are linearly independent, there is a unique solution to each of Eqs. (4.17)–(4.19). We now seek a single surface z^c which minimizes the sum of the mean square error:

$$E_\lambda(\mathbf{z}) = \lambda^2 \|\mathbf{I}\mathbf{z} - \mathbf{z}^m\|^2 + (1 - \lambda)^2 (\|\mathbf{T}_x \mathbf{z} + \mathbf{n}_x^c\|^2 + \|\mathbf{T}_y \mathbf{z} + \mathbf{n}_y^c\|^2) \quad (4.20)$$

where $\lambda \in [0, 1]$ is used to weight the relative importance of the measurements \mathbf{z}^m and \mathbf{n}^m to the error. This can be formulated as a matrix equation:

$$E_\lambda(\mathbf{z}) = \left\| \begin{bmatrix} \lambda \mathbf{I} \\ (1 - \lambda) \mathbf{T}_x \\ (1 - \lambda) \mathbf{T}_y \end{bmatrix} \mathbf{z} - \begin{bmatrix} \lambda \mathbf{z} \\ (\lambda - 1) \mathbf{n}_x^c \\ (\lambda - 1) \mathbf{n}_y^c \end{bmatrix} \right\|^2 \quad (4.21)$$

Where the minimizing $\mathbf{z}^c(\lambda)$ must fulfil the normal equations:

$$\begin{bmatrix} \lambda \mathbf{I} \\ (1 - \lambda) \mathbf{T}_x \\ (1 - \lambda) \mathbf{T}_y \end{bmatrix}^T \begin{bmatrix} \lambda \mathbf{I} \\ (1 - \lambda) \mathbf{T}_x \\ (1 - \lambda) \mathbf{T}_y \end{bmatrix} \mathbf{z}^c(\lambda) = \begin{bmatrix} \lambda \mathbf{I} \\ (1 - \lambda) \mathbf{T}_x \\ (1 - \lambda) \mathbf{T}_y \end{bmatrix}^T \begin{bmatrix} \lambda \mathbf{z} \\ (\lambda - 1) \mathbf{n}_x^c \\ (\lambda - 1) \mathbf{n}_y^c \end{bmatrix} \quad (4.22)$$

³Since \mathbf{z} has been reshaped to a vector, \mathbf{T}_x and \mathbf{T}_y are formed such that the output is the same as if these kernels were applied to \mathbf{Z} before reshaping.

Solving this system directly is inefficient as the left-hand matrix is sparse before being multiplied with its transpose. Instead, we solve the system using the sparse least squares solver built in to *Matlab*. In the least squares system (i.e. Eq. (4.22) without the transpose matrix) the left-hand matrix is $3p \times p$ with $13p$ nonzero elements. Figure 4.9 shows $z^c(\lambda)$ after being reshaped into a matrix $\mathbf{Z}^c(\lambda)$ for several λ . Figure 4.9a ($\lambda = 0$) is especially noteworthy as it produces an approximation to \mathbf{Z} without using the disparity data. Thus, this case is a crude realisation of a purely photometric stereo height reconstruction.

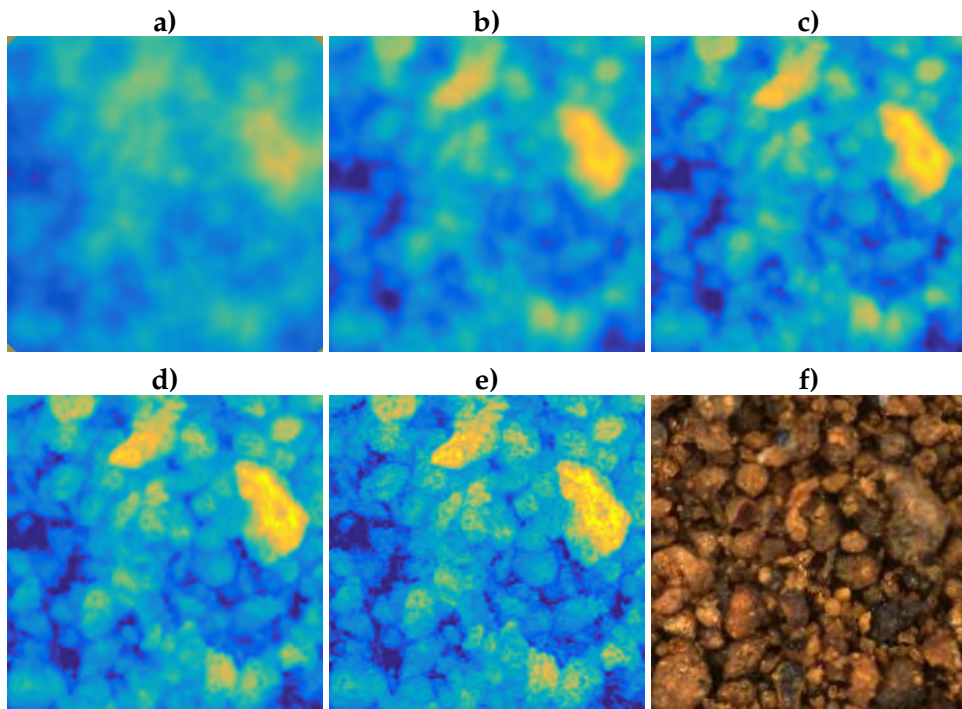


Figure 4.9: $\mathbf{Z}^c(\lambda)$ for different weights. **a)-e)** use $\lambda = 0, .05, .1, .2, .4$ respectively. **f)** shows a colour image of the scene.

5 Data analysis

This chapter serves to highlight some of the possible analyses which can be made using our 3D microscopy data. Discussions with scientists are ongoing about the future direction of this. Appendix A shows these methods applied to several regolith simulants.

5.1 Visually apparent data

A strength of our approach is the intuition of the raw data. In certain fields, such as geology, a major tool is visual cues from images or charts. Additionally, these cues are ripe territory for machine vision and learning algorithms to be applied if automation is desired. Considering e.g. Figure 2.7 there are several immediate observations to be made:

- The individual particle size, count, and shape.
- The individual texture.
- The individual specularity (especially corresponding to metallic or crystalline material).
- The macrocomposition (e.g. there is mostly brown rocks, with a small number of black and a few more grey rocks).

These properties form the fundamental terramechanics of a material, which has important applications in science and mission operations. This includes understanding the formation of surface features and deciding on immediate hazard of embedment or long-term wear in an area. The wealth of this data is emphasised when viewed in 3D using virtual reality or stereoscopic pairs. If these methods are not available, playback of multi-view images in rapid succession is sufficient for a human to perceive the depth of the images.

5.2 Particle size in z-direction

The particle size in the z -direction can be estimated from the data by computing the protrusion of each object compared to the plane in which it lies. To create this mean plane, the height map is averaged using a large-radius Gaussian filter. For most samples, this corresponds to a flat plane near $z = 0$, but if a sample is globally uneven or skewed this plane will adapt. A measure of the object size in z is found by taking twice (since half of a rock is beneath the

plane) the mean height or RMS height of every pixel compared to the mean plane.

5.3 Void fraction

The fraction of the scene which is empty (or void) can be calculated as well. Take the mean plane from Section 5.2 and shift it upwards until it touches the tallest peak of the sample. Measure the void volume beneath this shifted plane and the sample height surface. Then shift the plane downwards until it touches the deepest trough of the sample, the volume between the two planes is the reference volume for the fraction.

5.4 Specularity

The specularity of a sample can be detected by comparing the input images in the CIM dataset to a corresponding Lambertian image reconstructed with Eq. (4.8) and the normal vectors calculated from photometric stereo in Section 4.2. The specularities are detected by subtracting the Lambertian image from the real image and thresholding the result. This is repeated for each light source in the CIM dataset and the total specularity is found, see Figure 5.1.

This method is a first step towards our more ambitious goal of measuring photometric properties using the microscope developed in this thesis. Since we have control of both the illumination and viewing direction it effectively forms a gainoreflectometer which can be used to model the bidirectional reflectance distribution function (BDRF) at every point in the microscopy image.

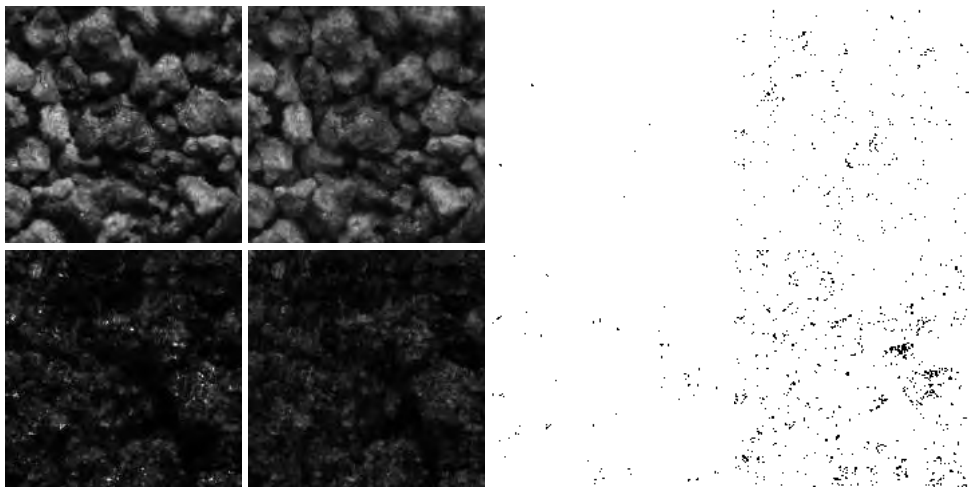


Figure 5.1: Comparison of specularities for JSC MARS-1 (top row) and JSC-1A (bottom row). From left to right: 1) Image captured using a single light source. 2) Reconstructed Lambertian image for this light source. 3) Specularities detected in the difference between the preceding images (negative). 4) Sum of specularities across all images in the CIM dataset (negative).

6 Miniaturised microscope

We demonstrate a miniaturised and optically similar microscope to the bench demonstrator. It measures $6 \times 6 \times 8 = 288 \text{ cm}^3$ and weighs 136 grams assembled. It is constructed from plastic by a hobby-grade fused deposition modelling (FDM) 3D-printer. Many components are retained between the two but the following changes are made:



Figure 6.1: Deployed projectile mock-up microscope.



Figure 6.2: Assembled and connected optics.

- Camera replaced with an Imaging Development Systems (IDS) uEye UI-5254LE 1/1.8" CMOS (1600 × 1200 pixels, 4.5 μm each, 10-bit).
- Tube lens replaced with a Fujinon HF50HA-1B ($f_t = 50$ mm, $a_t = 22$ mm).
- Objective lens replaced with an Edmund Optics (EO) #49-656 Aspherized Achromat ($f_o = 12$ mm, $a_o = 8$ mm).

The key parameters of the microscope remain unchanged. In particular the magnification is still $M = 50/12 = 4.17$ and the object plane pixel size is essentially unchanged at $4.5 \mu\text{m}/4.17 = 1.08 \mu\text{m}$. Figure 6.4 shows that the useful aperture size at the LCD also remains constant. With such similar properties we can immediately transplant the methods developed for our bench demonstrator microscope and assert that the output data is equally poignant, despite the small size. Figure 6.3 shows an example scene captured with the miniature microscope and a height reconstruction by direct application of Section 4.1.

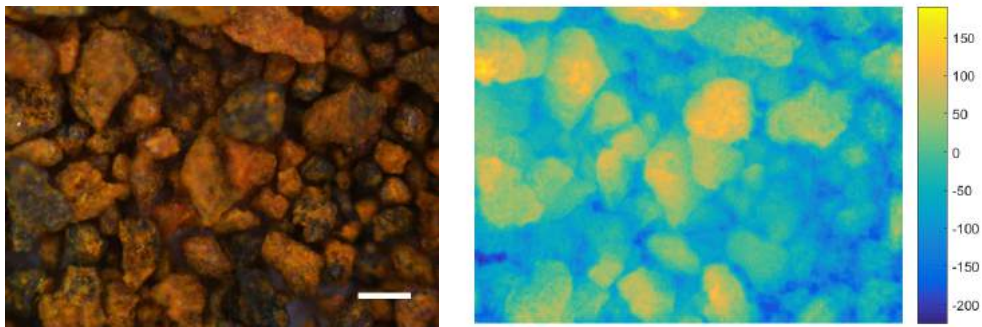


Figure 6.3: Example image and reconstruction from the miniaturised microscope. Left: 1530 × 1130 colour image, 2 mm aperture, 200 μm scale bar. Right: Reconstructed height using 7 aperture pattern, units of micrometre.

This miniaturised microscope has several applications in current and proposed planetary exploration, including mounted to a robotic arm, or on the belly of a helicopter. One particular application is demonstrated by integrating this prototype into an 82 mm diameter projectile mock-up corresponding to the SPEARS prototype launcher. This projectile is also 3D-printed and fitted with a clear plastic dome to show the optics inside, seen in Figure 6.1. Orienting the microscope can be completed by a turntable placed between the microscope and the finned base of the projectile. This microscope would be fully operational after integration of electronics similar to those of a modern cellular phone, which provides ample processing power, networking, and battery life for the system.

6.1 Future development

We are confident that the miniaturised microscope can be developed into a rugged system for use in SPEARS and other high-impact applications. Impact resistant cameras are commonplace for action sports photography (e.g. GoPro). The major improvements necessary, which can be implemented using semi-custom commercial parts, are:

- The glass LCD needs to be replaced with a plastic-LCD or organic-LCD model, preferably with improved contrast to the prototype. These are commercially available and marketed as indestructible.¹
- The optics need to be strengthened. The best results are likely achieved by combining ruggedised mountings² with plastic lenses.³ In this step, the optics should also be optimised to provide a flatter focal plane, wider maximum aperture, and higher possible resolution.
- Data capture needs to be integrated, e.g. using a microcontroller designed for embedded or cellular phone applications.

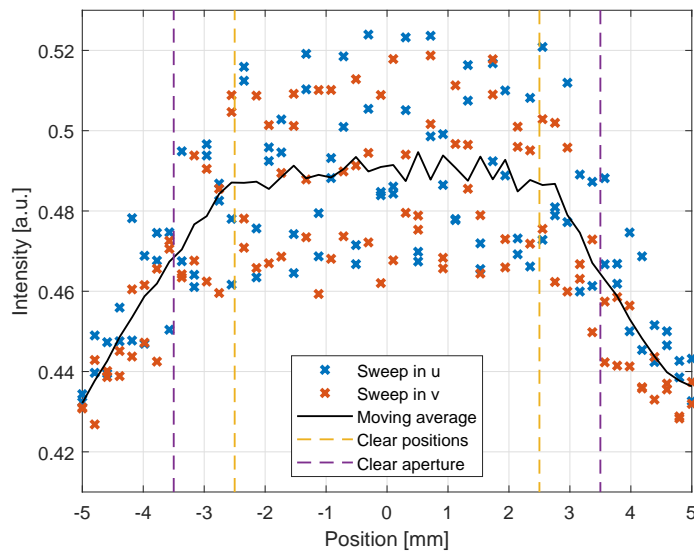


Figure 6.4: Measurement of alignment and size of the miniaturised microscope aperture. The same methods as for the bench microscope (Figure 3.6) were applied here. The clear aperture is measured to $a = 7$ mm.

¹E.g. EM Flexible Plastic LCD

²E.g. Edmund Optics Cr Series Fixed Focal Length Lenses

³E.g. Edmund Optics Plastic Aspheric Lenses

7 Conclusions and future work

In this thesis, we have demonstrated and prototyped a small and simple 3D microscope. The raw data delivered is rich and intuitive, giving a human observer cues about an object's microstructure, macrocomposition, and packing. We especially consider the microscope as a tool for planetary exploration, studying e.g. surface regoliths in-situ, or delivered into extreme environments by various new concepts for exploration. Additionally, the 3D microscope is a practical instrument. We require no scoops, sieves, or precise treatment, but rather are happy being crudely dunked into any environment, and capturing the data from our solid-state instrument.

Perhaps the most important point to bring home is the value-to-resource proposition the demonstrated 3D microscope. Our commercial-off-the-shelf (COTS) miniaturised prototype fits in the palm of a hand and weighs in at roughly 100 grams. The resource requirements are not much different from carrying a simple camera itself, requiring only some additional power for the transparent LCD and the LEDs. Therefore we can already identify multiple roles the 3D microscope can serve on a mission. We consider for example adding this device to the robotic arm of a current rover, serving as a fast tool to evaluate a sample, and if further study is carried out with specialised instruments, as an important source of context to these measurements.

As the main contribution of this thesis is novel engineering work, we have so far only implemented basic methods for data capture and analysis that do not make the ultimate capabilities of our hardware justice. Throughout this thesis, several exciting paths of future work has been discussed. In the short term we wish to apply multiplexed control of the programmable aperture [Liang et al., 2008], and extend the illumination to continuously variable gradient methods [Francken et al., 2008], which will enable faster and better reconstruction of both light-field and normal vector fields, and thus provide more detailed 3D data, powerful rendering capabilities, and deeper analysis. Another key short-term development is to vary illumination direction and perspective all at once, to capture the BDRF of our samples and thus produce datasets for identifying materials and understanding composition. In the longer term, we hope to close the loop between illumination and aperture control. Illumination and imaging are intimately connected, and it would be no surprise if iterative computational methods to leverage this fact can take this novel hardware to uses we cannot foresee today.

The device we have created is admittedly of a low Technology Readiness Level (TRL). However, we are confident the system can quickly reach a high TRL with more engineering work, as it was created using only COTS parts and is a straightforward design. This is especially true for the more sober applications we have considered, such as robotic arm delivery. As discussed in Section 6.1, more significant steps are necessary to enable a resistant design for SPEARS or other hard-impact applications. We stress that there is prior work on impact resistant LCDs, cameras, and optics which are commercially available today; hard-impact applications are not that far-fetched.

There is a wide variety of variations to our broader 3D microscopy concept with specialised purposes. For instance, by complementing the white LEDs with ultraviolet variants, the microscope is augmented to search for fluorescence bio-signatures, much like Curiosity's MAHLI [Edgett et al., 2012]. A modification which more fundamentally changes the behaviour would be to remove the first polarisation filter in the LCD. This modification would functionally alter the LCD from a virtual aperture to a tunable polarisation filter, effectively creating a polarisation microscope.

There is no reason to think the benefits we bring to exploration cannot be applied to our home planet as well. Consider for example placing the 3D microscope in a handheld box with a computer, display, and battery for field inspection. It would allow geologists back on earth to get a much closer, and deeper, look than the ubiquitous hand-lens in a roughly 500-gram hand-held device. Perhaps similar benefits can be found in manufacturing or structural inspections.

At the end of the day, I hope you take this home from my thesis: the small and simple 3D microscope we have demonstrated has an unexpectedly rich output. There is no magic or outlandish technology which makes it tick, but common optics and electronics. Why should we not pursue this further?

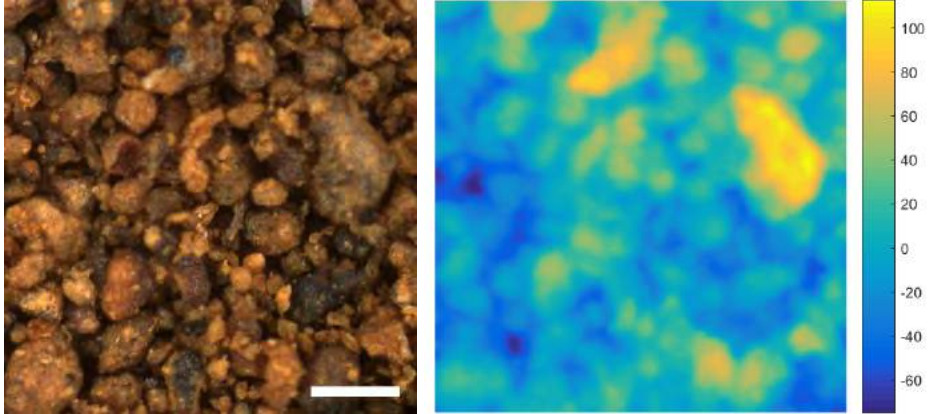
A Regolith measurement data

This chapter shows data for several different regolith simulants. JSC-1A (Moon) and JSC MARS-1 contain particles of various sizes. For these, subsets of particles in three size classes have been imaged. The other simulants are both lunar and have been milled into very fine particles. For each simulant the following is provided:

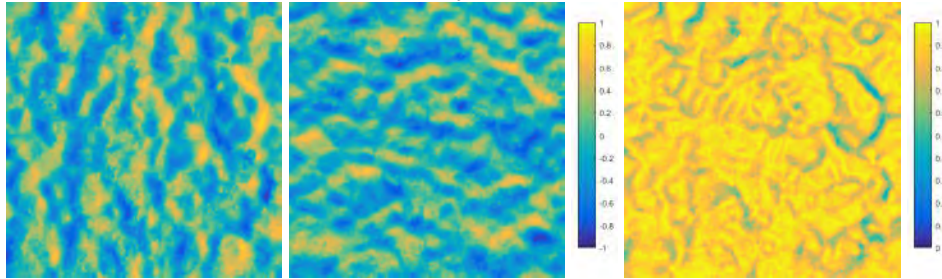
- A colour image with all lights on, a 1.5 mm aperture, and a calibrated scale bar.
- A corrected and calibrated height map, \mathbf{Z}^c .
- The corrected normal vectors \mathbf{N}^c .
- A 3D rendering of the recovered surface.
- Each of the four analysis data from Chapter 5.

A.1 JSC MARS-1 (small particles)

Left: Image with 200 μm scale bar. Right: Z^c in μm :



N_x^c , N_y^c , and N_z^c :



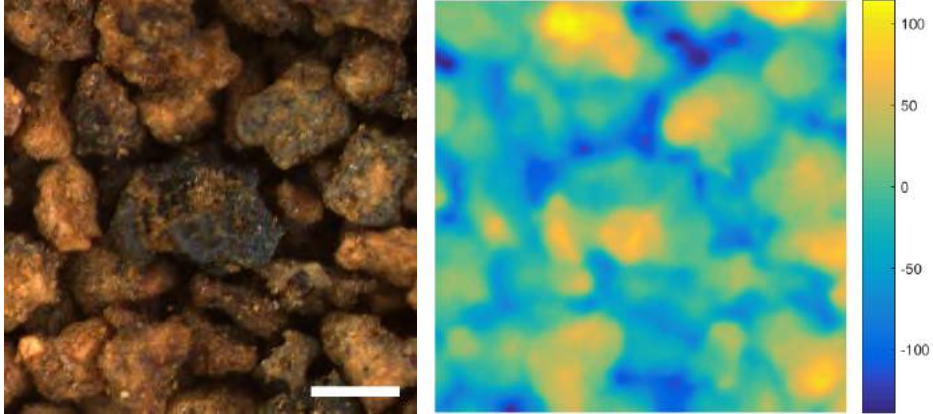
3D rendering:



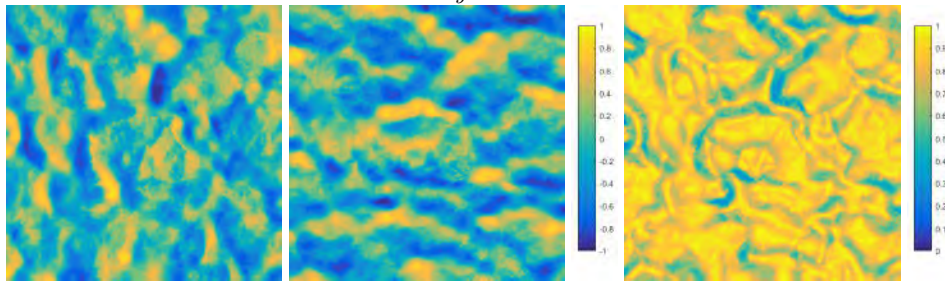
Void: 54%
Specularity: 1.2%
SD height: 50 μm
Mean height: 39 μm

A.2 JSC MARS-1 (medium particles)

Left: Image with 200 μm scale bar. Right: Z^c in μm :



N_x^c , N_y^c , and N_z^c :



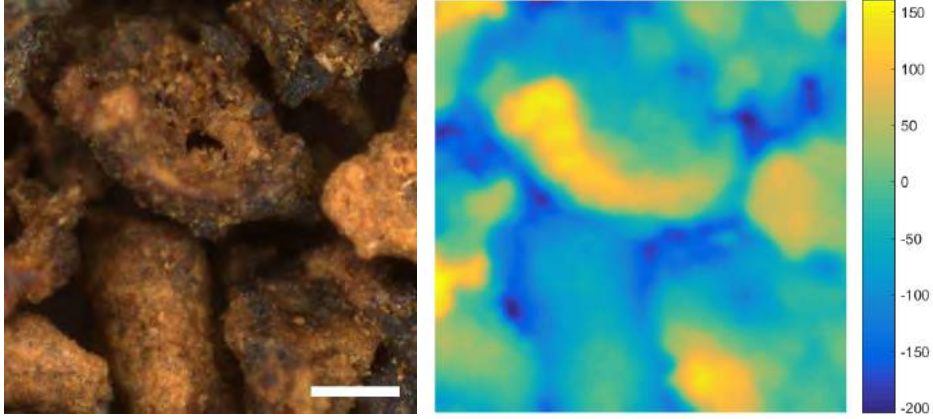
3D rendering:



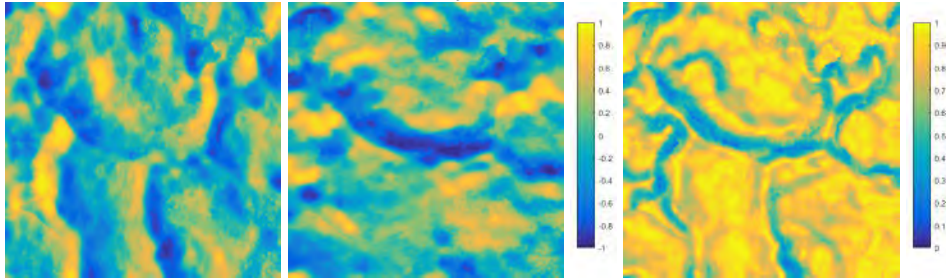
Void: 48%
Specularity: 1.7%
SD height: 79 μm
Mean height: 62 μm

A.3 JSC MARS-1 (large particles)

Left: Image with 200 μm scale bar. Right: Z^c in μm :



N_x^c , N_y^c , and N_z^c :



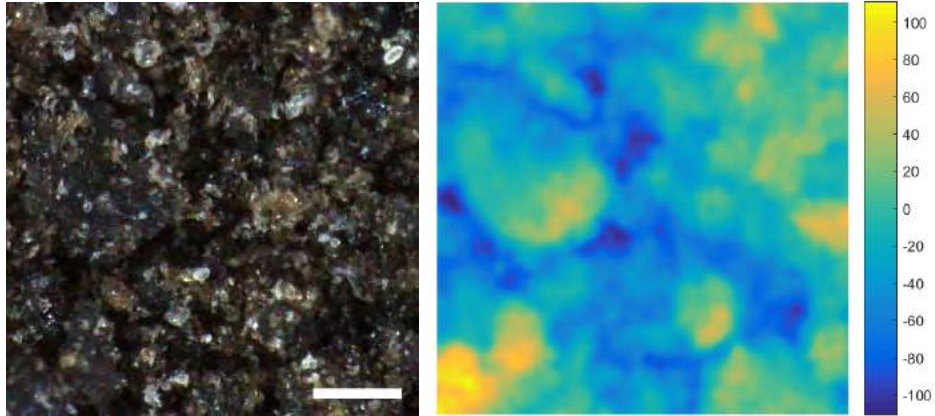
3D rendering:



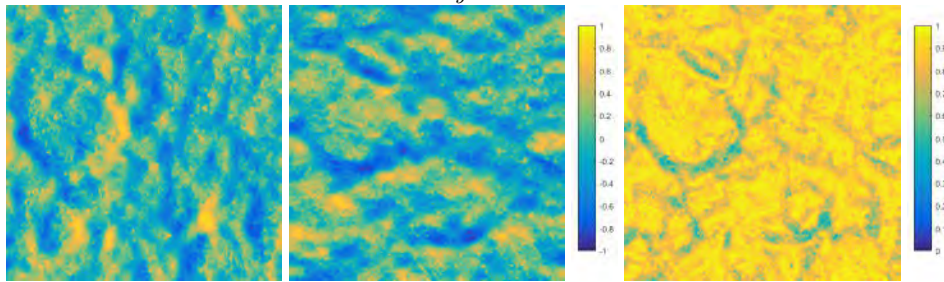
Void: 52%
Specularity: 1.1%
SD height: 120 μm
Mean height: 94 μm

A.4 JSC-1A (small particles)

Left: Image with 200 μm scale bar. Right: Z^c in μm :



N_x^c , N_y^c , and N_z^c :



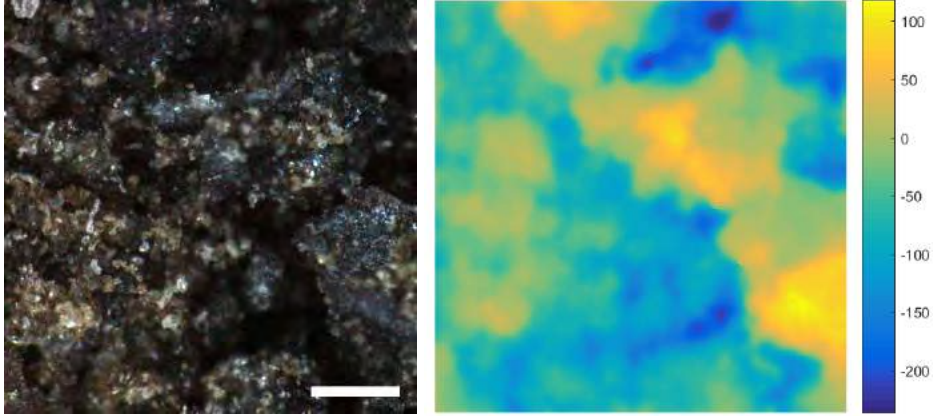
3D rendering:



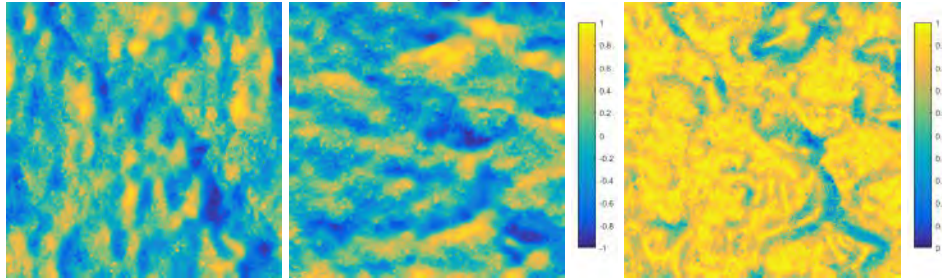
Void: 57%
Specularity: 3.5%
SD height: 55 μm
Mean height: 43 μm

A.5 JSC-1A (medium particles)

Left: Image with 200 μm scale bar. Right: Z^c in μm :



N_x^c , N_y^c , and N_z^c :



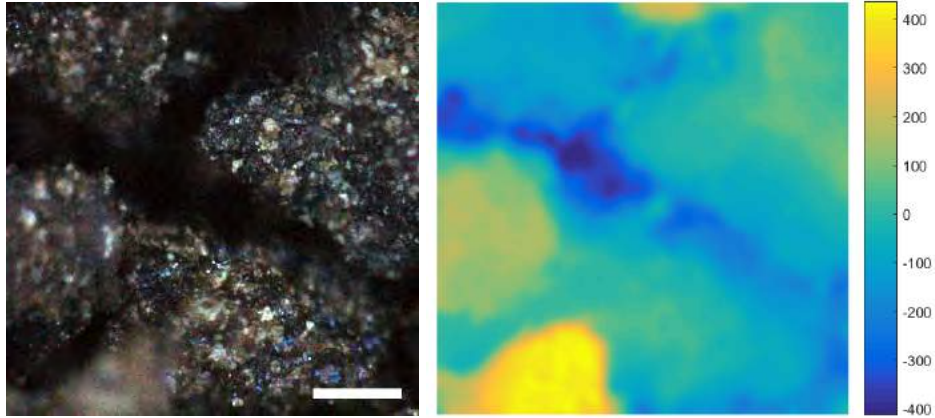
3D rendering:



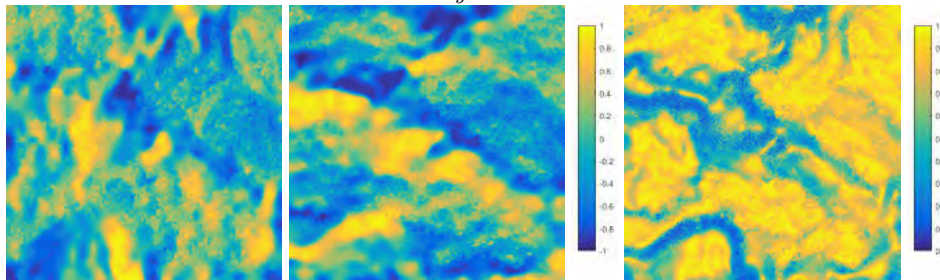
Void: 40%
Specularity: 3.4%
SD height: 92 μm
Mean height: 71 μm

A.6 JSC-1A (large particles)

Left: Image with 200 μm scale bar. Right: Z^c in μm :



N_x^c , N_y^c , and N_z^c :



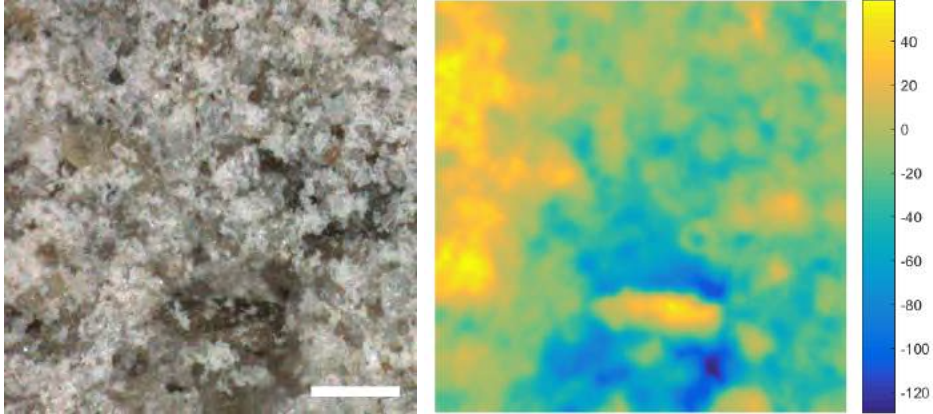
3D rendering:



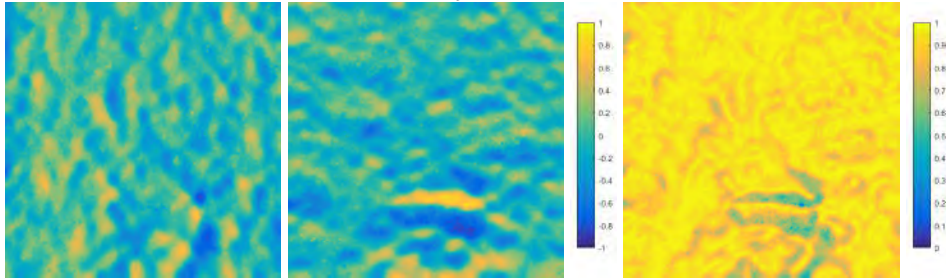
Void: 50%
Specularity: 2.4%
SD height: 189 μm
Mean height: 140 μm

A.7 NU-LHT-2M (finely milled)

Left: Image with 200 μm scale bar. Right: Z^c in μm :



N_x^c , N_y^c , and N_z^c :



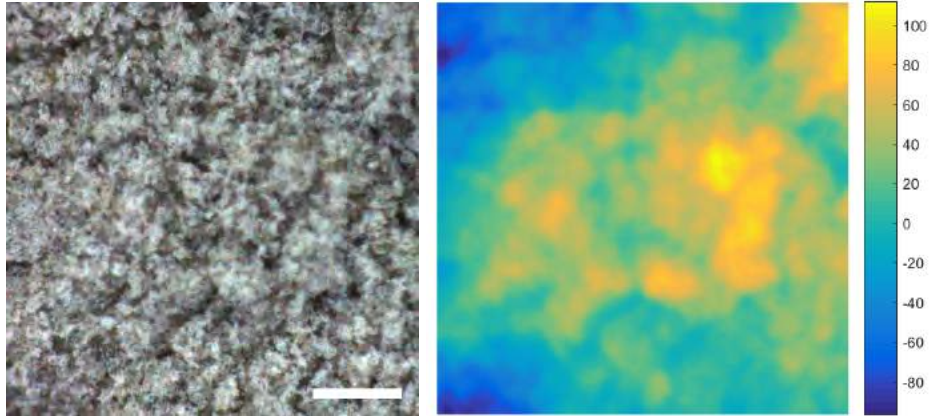
3D rendering:



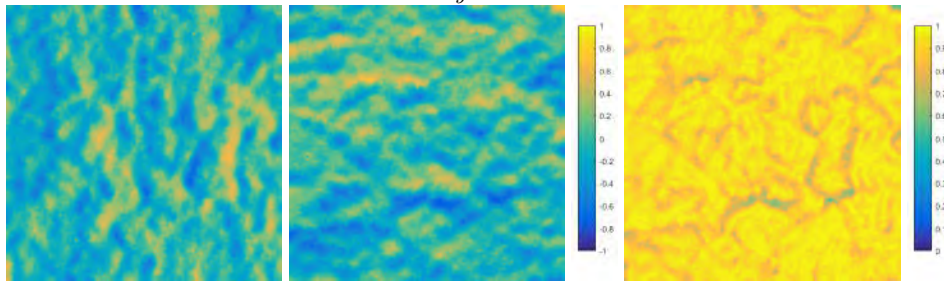
Void: 53%
Specularity: 1.4%
SD height: 41 μm
Mean height: 29 μm

A.8 RPBL (finely milled)

Left: Image with 200 μm scale bar. Right: Z^c in μm :



N_x^c , N_y^c , and N_z^c :



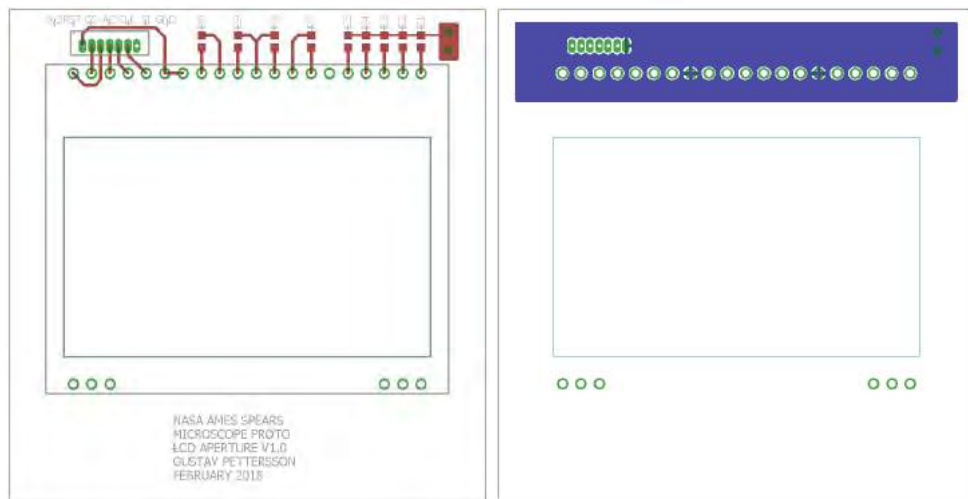
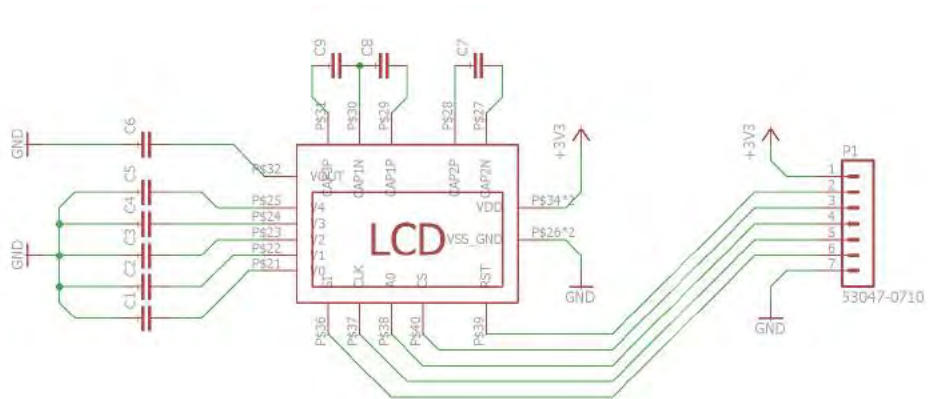
3D rendering:



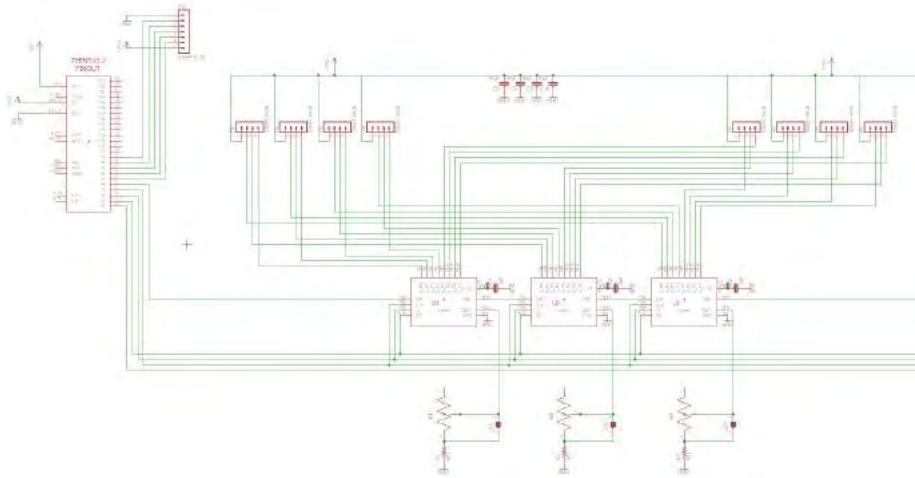
Void: 49%
Specularity: 1.3%
SD height: 36 μm
Mean height: 28 μm

B Schematics and PCBs

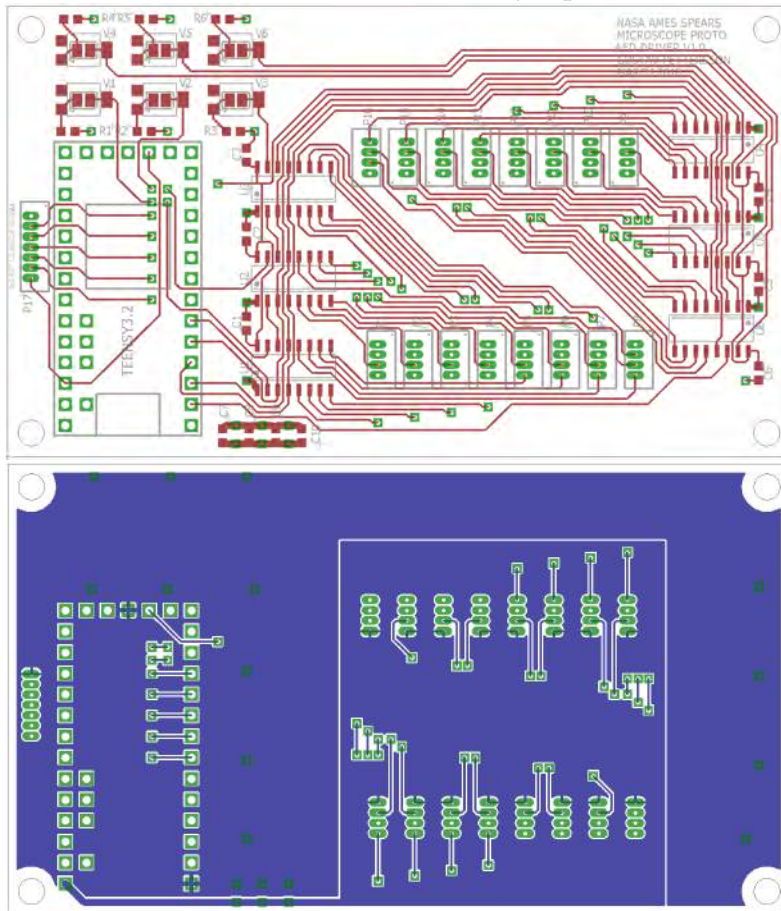
B.1 LCD holder



B.2 Control electronics



The set of three LED drivers is identically repeated once more.



Bibliography

- Edmund Optics Plastic Aspheric Lenses. URL <https://www.edmundoptics.com/optics/optical-lenses/aspheric-lenses/Plastic-Aspheric-Lenses/>. Accessed: 30 May 2018.
- Edmund Optics Cr Series Fixed Focal Length Lenses. URL <https://www.edmundoptics.com/imaging-lenses/fixed-focal-length-lenses/cr-series-fixed-focal-length-lenses/>. Accessed: 30 May 2018.
- EM Flexible Plastic LCD. URL <http://www.emmicroelectronic.com/products/display-touch/flexible-plastic-lcd/flexible-plastic-lcd>. Accessed: 30 May 2018.
- S. Abrahamsson, J. Chen, B. Hajj, S. Stallinga, A. Y. Katsov, J. Wisniewski, G. Mizuguchi, P. Soule, F. Mueller, C. D. Darzacq, X. Darzacq, C. Wu, C. I. Bargmann, D. A. Agard, M. Dahan, and M. G. L. Gustafsson. Fast multicolor 3D imaging using aberration-corrected multifocus microscopy. *Nature Methods*, 10(1), December 2012. ISSN 1548-7091.
- U. J. Birk. *Super-Resolution Microscopy - A Practical Guide*. John Wiley & Sons, Inc, 2017. ISBN 3-527-80206-1.
- A. Bovik. *The essential guide to image processing*. Elsevier/AP, 2009. ISBN 1-282-16876-2.
- J. Bruce. *Design, Building, Testing, and Control of SUPERball: A Tensegrity Robot to Enable New Forms of Planetary Exploration*. PhD thesis, UC Santa Cruz, 2016.
- D. E. Buetow. *Three-dimensional confocal microscopy volume investigation of biological specimens*. Cell biology. Academic Press, 1994. ISBN 0-323-13896-9.
- A. Datta, B. Roget, D. Griffiths, G. Pugliese, J. Sitaraman, J. Bao, L. Liu, and O. Gamard. Design of a Martian Autonomous Rotary-Wing Vehicle. *Journal of Aircraft*, 40(3):461 – 472, 2003. doi: 10.2514/2.3141.
- M. W. Davidson and M. Abramowitz. *Optical Microscopy*. American Cancer Society, 2002. ISBN 9780471443391. doi: 10.1002/0471443395.img074.
- P. Eaton and P. West. *Atomic Force Microscopy*. Oxford University Press, March 2010. ISBN 0199570450.

- K. S. Edgett, R. A. Yingst, M. A. Ravine, M. A. Caplinger, J. N. Maki, F. T. Ghaemi, J. A. Schaffner, J. F. B. III, L. J. Edwards, K. E. Herkenhoff, E. Heydari, L. C. Kah, M. T. Lemmon, M. E. Minitti, T. S. Olson, T. J. Parker, S. K. Rowland, J. Schieber, R. J. Sullivan, D. Y. Sumner, P. C. Thomas, E. H. Jensen, J. J. Simmonds, A. J. Sengstacken, R. G. Willson, and W. Goetz. Curiosity's Mars Hand Lens Imager (MAHLI) Investigation. *Space Science Reviews*, 170(1-4):259–317, 2012.
- S. Favaro, Paolo; Soatto. *3-D Shape Estimation and Image Restoration : Exploiting Defocus and Motion Blur*. Springer, March 2007. ISBN 9781846281761.
- Y. Francken, C. Hermans, T. Cuypers, and P. Bekaert. Fast Normal Map Acquisition Using an LCD Screen Emitting Gradient Patterns. In *2008 Canadian Conference on Computer and Robot Vision*, pages 189–195, May 2008.
- A.-M. Harri, K. Pichkadze, L. Zeleny, L. Vazquez, W. Schmidt, S. Alexashkin, O. Korablev, H. Guerrero, J. Heilimo, M. Uspensky, V. Finchenko, V. Linkin, I. Arruego, M. Genzer, A. Lipatov, J. Polkko, M. Paton, H. Savijärvi, H. Haukka, T. Siili, V. Khovanskov, B. Ostesko, A. Poroshin, M. Diaz-Michelena, T. Siikonen, M. Palin, V. Vorontsov, A. Polyakov, F. Valero, O. Kemppinen, J. Leinonen, and P. Romero. The MetNet vehicle: a lander to deploy environmental stations for local and global investigations of Mars. *Geoscientific Instrumentation, Methods and Data Systems*, 6(1):103–124, 2017. doi: 10.5194/gi-6-103-2017.
- K. E. Herkenhoff, S. W. Squyres, J. F. Bell, J. N. Maki, H. M. Arneson, P. Bertelsen, D. I. Brown, S. A. Collins, A. Dingizian, S. T. Elliott, W. Goetz, E. C. Hagerott, A. G. Hayes, M. J. Johnson, R. L. Kirk, S. McLennan, R. V. Morris, L. M. Scherr, M. A. Schwochert, L. R. Shiraishi, G. H. Smith, L. A. Soderblom, J. N. Sohl-Dickstein, and M. V. Wadsworth. Athena Microscopic Imager investigation. *Journal of Geophysical Research: Planets*, 108(E12), 2003. doi: 10.1029/2003JE002076.
- S. D. Howe, R. C. O'Brien, R. M. Ambrosi, B. Gross, J. Katalenich, L. Sailer, M. McKay, J. C. Bridges, and N. P. Bannister. The Mars Hopper: an impulse driven, long range, long-lived mobile platform utilizing in-situ Martian resources. *Acta Astronautica*, 69(11):1050–1056, 2011.
- R. L. Kirk, E. Howington-Kraus, B. Redding, D. Galuszka, T. M. Hare, B. A. Archinal, L. A. Soderblom, and J. M. Barrett. High-resolution topomapping of candidate MER landing sites with Mars Orbiter Camera narrow-angle images. *Journal of Geophysical Research: Planets*, 108(E12), 2003. doi: 10.1029/2003JE002131.

- M. Levoy and P. Hanrahan. Light Field Rendering. In *Proceedings of the 23rd Annual Conference on Computer Graphics and Interactive Techniques, SIGGRAPH '96*, pages 31–42. ACM, 1996. ISBN 0-89791-746-4. doi: 10.1145/237170.237199.
- M. Levoy, R. Ng, A. Adams, M. Footer, and M. Horowitz. Light Field Microscopy. In *ACM SIGGRAPH 2006 Papers, SIGGRAPH '06*, pages 924–934. ACM, 2006. ISBN 1-59593-364-6. doi: 10.1145/1179352.1141976.
- C.-K. Liang, T.-H. Lin, B.-Y. Wong, C. Liu, and H. H. Chen. Programmable Aperture Photography: Multiplexed Light Field Acquisition. In *ACM SIGGRAPH 2008 Papers, SIGGRAPH '08*, pages 55:1–55:10. ACM, 2008. ISBN 978-1-4503-0112-1. doi: 10.1145/1399504.1360654.
- NASA. Mars Helicopter to Fly on NASA's Next Red Planet Rover Mission, May 2018. URL <https://www.nasa.gov/press-release/mars-helicopter-to-fly-on-nasa-s-next-red-planet-rover-mission>.
- D. Nehab, S. Rusinkiewicz, J. Davis, and R. Ramamoorthi. Efficiently Combining Positions and Normals for Precise 3D Geometry. In *ACM SIGGRAPH 2005 Papers, SIGGRAPH '05*, pages 536–543. ACM, 2005. doi: 10.1145/1186822.1073226.
- R. Ng, M. Levoy, M. Bredif, G. Duval, M. Horowitz, and P. Hanrahan. Light Field Photography with a Hand-held Plenoptic Camera. *Stanford Tech Report, CTSR 2005-02*, 2005. URL <http://graphics.stanford.edu/papers/lfcamera/lfcamera-150dpi.pdf>.
- U. of Central Florida CLASS. Planetary Simulant Database: JSC Mars-1/1A. URL http://sciences.ucf.edu/class/simulant_jscmars1/. Accessed: 30 May 2018.
- Y. Schechner and N. Kiryati. Depth from Defocus vs. Stereo: How Different Really Are They? *International Journal of Computer Vision*, 39(2):141–162, September 2000.
- I. Sobel. History and Definition of the so-called "Sobel Operator", more appropriately named the Sobel-Feldman Operator, 2014. URL https://www.researchgate.net/publication/239398674_An_Isotropic_3x3_Image_Gradient_Operator. First presented at the Stanford Artificial Intelligence Project (SAIL), 1968.
- K. R. Spring and M. W. Davidson. Depth of Field and Depth of Focus. URL <https://www.microscopyu.com/microscopy-basics/depth-of-field-and-depth-of-focus>. Accessed: 30 May 2018.

- O. C. Wells. *Scanning electron microscopy*. McGraw-Hill, 1974. ISBN 0-07-069253-x.
- D. R. Williams. Chronology of Lunar and Planetary Exploration, May 2018. URL <https://nssdc.gsfc.nasa.gov/planetary/chronology.html>. Accessed: 30 May 2018.
- U. Wong. *Lumenhancement: Exploiting Appearance for Planetary Modeling*. PhD thesis, Carnegie Mellon University, 2012.
- R. J. Woodham. Photometric Method For Determining Surface Orientation From Multiple Images. *Optical Engineering*, 19(1):139–144, 1980. doi: 10.1117/12.7972479.